



High loads of rare earth single-atom lanthanum anchored carbon nitride with special double-layer coordination structure for efficient photocatalysis

Linlin Sun^a, Xiaoshuo Liu^b, Yibing Feng^a, Xunlei Ding^c, Jigang Wang^{a,*}, Nan Jiang^{d,*}, Shanjiang Wang^{e,*}

^a Jiangsu Key Laboratory of Advanced Metallic Materials, School of Materials Science and Engineering, Southeast University, Nanjing 211189, PR China

^b School of Energy and Power Engineering, North China Electric Power University, Baoding 071003, PR China

^c Institute of Clusters and Low Dimensional Nanomaterials, School of Mathematics and Physics, North China Electric Power University, Beijing 102206, PR China

^d Collaborative Innovation Center for Cardiovascular Disease, Translational Medicine of Jiangsu, School of Pharmacy, Nanjing Medical University, Nanjing 211166, PR China

^e School of Materials Science and Engineering, Nanjing Tech University, Nanjing 210009, PR China

ARTICLE INFO

Keywords:

Rare earth single-atom lanthanum
Hierarchical agaric-like carbon nitride
Spatial coordination configuration
Activation of molecular oxygen
Photocatalytic

ABSTRACT

A special two-layer coordination configuration anchored single-atom La (SALa) catalyst is synthesized to realize the effective separation of electrons in space and efficient active sites for the activation of O₂ to produce more active species. The special SALa microenvironment is obtained by a novel and facile reduction method that avoids the formation of rare earth oxides and the concentration of loaded SALa (10.34 wt%) exceeds that in most previous studies. The photodegradation test results show that antibiotics are almost completely removed within 30 min by SALa/CN. The first-order kinetic constant of SALa/CN (0.10661 min⁻¹) is approximately 9.81 times higher than that of 3DA-CN (0.01087 min⁻¹). SALa can be considered as a bridge to transfer electrons and •O₂⁻, ¹O₂ and h⁺ are the main active species to degrade tetracycline into some pollution-free small molecules. This work provides an efficient rare earth single-atom catalyst activity strategy possessing certain potential in practical applications.

1. Introduction

Many kinds of diseases triggering human beings can be effectively treated with antibiotics and the breeding industry excessively depends on them. What worries people is that the majority of antibiotics cannot be completely absorbed by the human body. Approximately 90% of antibiotics are discharged into the environment in the form of the origin or metabolites of the body [1–3]. Moreover, the continuous pollution of antibiotics poses a great threat to the ecological environment and human health. Self-degrading antibiotics using solar energy under natural conditions is a promising technology to solve the above problems, which has the advantages of strong oxidation capacity, easy implementation and green environmental protection [4–6]. In the process of self-degradation, the photocatalyst is irradiated by an energy greater than or equal to the band gap of the photocatalyst, triggering the production of photogenerated electrons (e⁻) and holes (h⁺) with certain energy [7,8]. The e⁻ and h⁺ are migrated in the interior and interface of the photocatalyst and undergone redox reactions with substances

adsorbed on the surface or in solvents, consequently, the active species are produced to act on antibiotics [9,10]. Regarding photocatalytic technology, the design of high-performance materials plays a decisive role in the application of photocatalytic treatment for antibiotics.

For traditional nanomaterials, most of the inner atoms cannot participate in the redox reaction and only the exposed surface atoms are involved in catalytic reactions, which has certain limitations for the utilization of active atoms. Single atom catalysts (SACs) have 100% atomic utilization providing the conditions for a single atom to fully contact the target molecules [11,12]. To date, many SACs with excellent performance have been reported in the field of photocatalysis. Wang et al. [13] proposed the photoinduction of single-atom Cu decorated on UiO-66-NH₂ for enhanced photocatalytic reduction of CO₂ forming liquid fuels. Sun et al. [14] constructed single-atom Ag decorated tremella-like g-C₃N₄, which significantly improved the photocatalytic efficiency of tetracycline (TC) removal. Single-atom Pt confined by the interlayer nanospace of g-C₃N₄ for efficient photocatalytic hydrogen evolution was researched by Quan's group [15]. Consequently, SACs can

* Corresponding authors.

E-mail addresses: wangjigang@seu.edu.cn (J. Wang), jiangnan@njmu.edu.cn (N. Jiang), sj_wang@njtech.edu.cn (S. Wang).

<https://doi.org/10.1016/j.apcatb.2023.122979>

Received 9 February 2023; Received in revised form 7 June 2023; Accepted 7 June 2023

Available online 23 June 2023

0926-3373/© 2023 Elsevier B.V. All rights reserved.

provide the large number of well-defined active sites for the reaction, which can maximize the catalytic activity of the photocatalyst [16–18].

Selecting suitable support material is the key step in obtaining SACs. Graphitic carbon nitride (g-C₃N₄) is a typical polymer semiconductor in which the C and N atoms in the structure form a highly delocalized π conjugated system with sp^2 hybridization. g-C₃N₄ has anions that coordinate with metal atoms and can design good coordination structures [19–21]. Gao et al. [22] explored the mechanism of single-atom Pd and Pt loading on g-C₃N₄ materials with excellent CO₂ reduction activity by DFT calculations. Zou's group [12] developed a highly active and stable SAAg/g-C₃N₄ sample, which can reduce the H₂ evolution barrier, expand the light absorption range and improve the charge transfer efficiency. Xiao et al. [23] established the engineering of single-atom Cu bonded with compositional N of g-C₃N₄, achieving highly effective charge transfer channels. Moreover, g-C₃N₄ with a two-dimensional nanosheet structure is prone to agglomeration, whereas hierarchical g-C₃N₄ can solve the agglomeration phenomenon and provide more active sites for the reaction. Therefore, it is expected that the SACs with hierarchical g-C₃N₄ as support material have excellent carriers separation efficiency, fantastic visible light absorption ability and high photocatalytic performance.

Among all kinds of SACs, rare earth SACs can realize efficient utilization and greatly improve the added value of rare earth resources. Rare earth elements have unique electronic, optical and magnetic properties arising from the spin-orbit coupling of the 4f and valence orbitals. In addition, benefiting from their electronic properties and large radii, rare earth atoms frequently present stable high-coordination structures which increase the thermal stability. Several rare earth SACs have recently been developed and exhibit excellent performance in various catalysis processes. Ma et al. [24] reported that praseodymium (Pr) SAC encapsulated by g-C₃N₄ substrate with a loading content of 21.05 wt% exhibited high photoreduction performance of CO₂ to CH₃OH. Shui's group [25] reported the synthesis of yttrium (Y, 0.38 wt%) and scandium (Sc, 1.24 wt%) SACs on N-doped carbon support for N₂ and CO₂ reduction reactions. Sun et al. [26] reported highly coordinated cerium (Ce, 0.26 wt%) single-atom sites on g-C₃N₄ nanosheets for efficient photocatalytic amine oxidation and H₂O splitting into H₂. However, the synthesis and application reports of rare earth SACs are still very limited. The 4f orbital of lanthanide (La) is not fully occupied, and the 5f orbital is vacant, which can provide effective electron capture capability, thus improving the separation efficiency of photoexcited carriers [27,28]. As a representative lanthanide compound, La has a shallow potential well induced by its full electron configuration, which can effectively regulate the electronic structure and catalytic activity of photocatalysts. Therefore, La has attracted extensive attention from researchers. Jia et al. [29] constructed La-doped ZnIn₂S₄ microspheres promoting the separation efficiency of electrons and holes. Jing et al. [30] prepared direct Z-scheme red g-C₃N₄/rod-like LaVO₄ composites with a remarkable enhancement of photocatalytic behaviour. Xie et al. [31] synthesized La₂O₃-modified g-C₃N₄ material with high specific surface area, extended light absorption and enhanced carriers separation efficiency. The above studies only introduced La as a doping element. However, single-atom La (SALa) catalysts have rarely been studied. Therefore, it is very valuable to obtain SALa material by simple and effective method. The nature of photocatalytic mechanism related to the electronic structure of rare earth single atom requires in-depth and systematic study at the atomic and electronic levels.

Herein, high loading of rare earth SALa on agaric-like g-C₃N₄ (3DA-CN) was prepared by solvothermal reduction combined with high-temperature reduction method achieving the maximum utilization rate of rare earth metal atoms and the utilization of effective added value. The new coordination configuration (two-layer structure) of SALa/CN is obtained, which reduces the transfer barrier of photogenerated electrons, and thus significantly increases the photocatalytic activity. The local environment of SALa/CN has been thoroughly studied by aberration-corrected high-angle annular dark field STEM (AC-HAADF-

STEM), X-ray absorption near edge structure (XANES) and extended X-ray absorption fine structure (EXAFS). The charge density distribution between SALa and 3DA-CN was studied by density functional theory (DFT) calculations. The time-resolved photoluminescence indicates that the main form of electrons transition for SALa/CN is nonradiative transition and that electrons mainly participate in the photocatalytic reaction. The steady-state fluorescence and photoelectric chemistry tests proved that SALa/CN has excellent carriers separation efficiency. In addition, SALa/CN was used in the photocatalytic removal of antibiotics showing excellent efficiency. The photocatalytic mechanism of the synergistic interaction between the electronic structure of rare earth SALa and 3DA-CN has been studied deeply and systematically.

2. Experimental section

2.1. Chemicals

Melamine (C₃H₆N₆), cyanuric acid (C₃H₃N₃O₃), lanthanum nitrate (La(NO₃)₃), ascorbic acid (C₆H₈O₆), isopropanol (C₃H₈O), 2,2,6,6-tetramethyl-1-piperidinyloxy (C₉H₁₈NO^{*}), 2,2,6,6-tetramethyl-4-piperidone (C₉H₁₇NO), 5,5-dimethyl-1-pyrroline N-oxide (C₆H₁₁NO) and catalase (CAT, 2000–5000 U/mg protein) were purchased from Aladdin Reagent. Acetonitrile (C₂H₃N), nitric acid (HNO₃), lanthanum oxide (La₂O₃), tetracycline (C₂₂H₂₄N₂O₈), oxytetracycline hydrochloride (C₂₂H₂₄N₂O₉-HCl), doxycycline hydrochloride (C₂₄H₃₀N₂O₉-HCl), ethanol (C₂H₆O), acetic acid (C₂H₄O₂) and sodium sulfate (Na₂SO₄) were supplied by Sinopharm Chemical Reagent. Ethylenediaminetetraacetic acid disodium salt (C₁₀H₁₄N₂Na₂O₈) and L-tryptophan (C₁₁H₁₂N₂O₂) were purchased from Jiuding Chemical Co., Ltd. All reagents were standard-grade analytical. Nitrogen (N₂) and hydrogen (H₂) were purchased from Nanjing Special Gas Co., Ltd. Deionized water was provided by a local water purification company.

2.2. Materials preparation

2.2.1. Synthesis of three-dimensional agaric-like carbon nitride (3DA-CN)

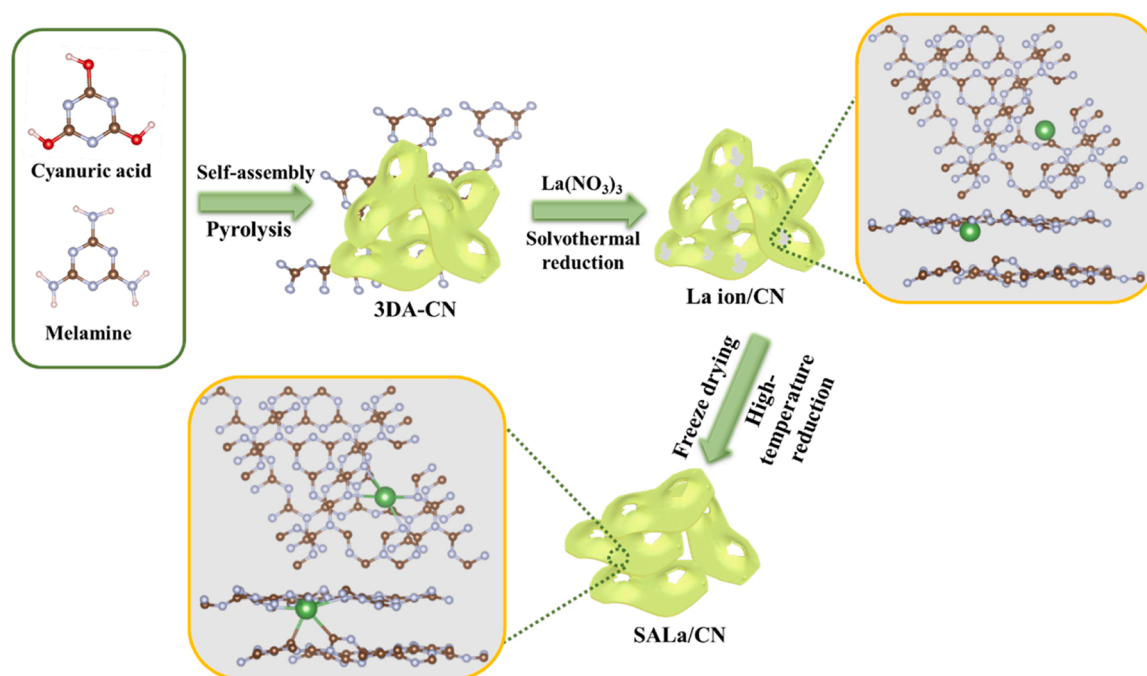
The 3DA-CN material was prepared by one-step direct calcination method. Specifically, 1:2:2 molar ratios of acetonitrile, ethanol and water were used to form a uniform mixed solution, and then melamine (1.26 g) and cyanic acid (1.29 g) were added to the above solution and stirred at room temperature for 4 h. After that, they were loaded into a high-pressure reaction kettle and kept at 110 °C for 12 h. After the reaction was cooled, the white supramolecular precursor was collected by centrifugation. The white product was dried and fully ground into fine powder and then put into the crucible and calcined directly in a muffle furnace, and the yellow powder was obtained, namely 3DA-CN.

2.2.2. Synthesis of single-atom lanthanum dispersed 3DA-CN (SALa/CN)

3DA-CN (0.2 g) was added to the deionized water (120 mL), and 3DA-CN was dispersed by ultrasound for 2 h. Then, La(NO₃)₃ (0.1 M, 15 mL) solution and an appropriate amount of phenol were added and ultrasonicated for 4 h under dark conditions. The mixed solution was put into the reaction kettle at 160 °C for 16 h. The reaction product was freeze-dried and then fully ground to obtain pale yellow fine powder (La ion/CN). The La ion/CN was put into the porcelain boat and calcined at 400 °C with H₂ and N₂ (V (H₂): V (N₂) = 3:17) for 4 h to obtain the product. Finally, the product was soaked and washed in water and ethanol to obtain the final sample (SALa/CN). A schematic illustration of the formation process of SALa/CN is depicted in Scheme 1.

2.3. Device characterization

The details of the device characterization are provided in the [supporting information](#) (SI).



Scheme 1. Schematic illustration of the formation process of SALa/CN.

2.4. Photocatalytic performance evaluation experiments

The photocatalytic performance of the as-prepared materials was evaluated by photocatalytic degradation TC. Specifically, 100 mL TC (20 mg/L) was added into the quartz reactor, and then 20 mg photocatalyst was added. The geometry of the reactor is cylindrical (outer height: 92 mm, external diameter: 70 mm, inner height: 78 mm, internal diameter: 46 mm). The reactor is designed with a double-layer jacket that is filled with circulating water (supplied by controlled temperature water circulation system) to maintain a constant temperature (25 °C) for the photocatalytic reaction. The dark reaction was performed under magnetic stirring for 30 min to achieve adsorption equilibrium and then the reaction was transferred into the photocatalytic system and the aeration device was started. The light source was 300 W Xenon lamp ($\lambda \geq 420$ nm), and reaction products were taken every 5 min. The liquid part of the reaction product was collected by centrifugation and filtration. The corresponding absorbance of the liquid was tested under UV–vis spectrophotometer at 357 nm. To ensure the reliability of the results, the same experiments were carried out three times. The Lambert–Beer law is used to calculate the degradation efficiency. To demonstrate the suitability of SALa/CN, photocatalytic removal of oxytetracycline and doxycycline was performed using the same experimental procedure as described above. The stability and effectiveness of SALa/CN were proven by using cycling experiments and simulating real water environment experiments.

3. Results and discussion

3.1. Morphology and microstructure analyses

The morphology and microstructure of 3DA-CN and SALa/CN were characterized by scanning electronic microscopy (SEM) and transmission electron microscopy (TEM). As shown in Fig. 1a, 3DA-CN shows an agaric-like structure with pores. To more clearly study the morphology of 3DA-CN, the scale of the image is enlarged in Fig. 1b. The morphology of 3DA-CN has a regular hierarchical structure consisting of undulating slices approximately 400 nm in size, providing the possibility of more active sites and multichannel electron transfer for the

reaction [32]. Moreover, a certain pore structure of 3DA-CN is found, which is conducive to mass transfer and diffusion to improve the catalytic activity [33]. It can be seen in Fig. 1c that the microstructure of 3DA-CN is more clearly displayed and presented almost transparent meaning thin thickness. The 3DA-CN shows an obvious three-dimensional structure similar to undulating agaric, which can shorten the distance of electrons transmission enhancing the separation efficiency of electrons and holes [34,35]. Moreover, the morphologies of SALa/CN are presented in Fig. 1d–e, which still maintain an agaric shape with unchanged pores. It indicates that the introduction of SALa does not change the morphology of 3DA-CN.

The tiny clusters or lanthanum-containing nanoparticles are not detected by TEM images (Fig. 1f–g), implying that La species are uniformly dispersed in the 3DA-CN matrix. Meanwhile, mapping images (Fig. 1h) were used to analyze the elemental composition (C, N and La) of SALa/CN. It verifies that C, N and La are uniformly dispersed throughout the SALa/CN. Due to the limitation of the detection sensitivity for TEM, the existence of SALa could not be clearly seen, so we carried out Aberration-corrected high-angle annular dark field STEM (AC-HAADF-STEM) to research the SALa/CN. As shown in Fig. 1i–j, the white bright spots (marked in yellow circles) are SALa, which clearly shows that the high-loading SALa are uniformly dispersed on the 3DA-CN without aggregation into clusters and nanoparticles. The intensity profiles along lines 1 and 2 further confirm that the size of these spots ranged from 1 Å to 2 Å and that there is a distance between bright spots, implying that each white spot is an isolated SALa [36]. Simultaneously, the loading content of SALa up to 10.34 wt% was detected by inductively coupled plasma optical emission spectroscopy (ICP–OES). Subsequently, the SALa/CN catalyst was soaked in nitric acid (0.5 mol/L) and then washed with water and ethanol. The content of La was detected by ICP–OES and it was found that the content of La (10.31 wt%) in the catalyst was almost not reduced. It indicates that the SALa/CN catalyst does not contain La_2O_3 and La clusters. Rare earth elements easily combine with ambient oxygen to form oxides, so it is difficult to obtain high load of rare earth SACs. The loading of SALa prepared in this experimental system is 10.34 wt%, which is higher than that of most previous rare earth SACs studies (Table S1). Therefore, the single-atom catalyst with high-loading of SALa was successfully obtained, laying a

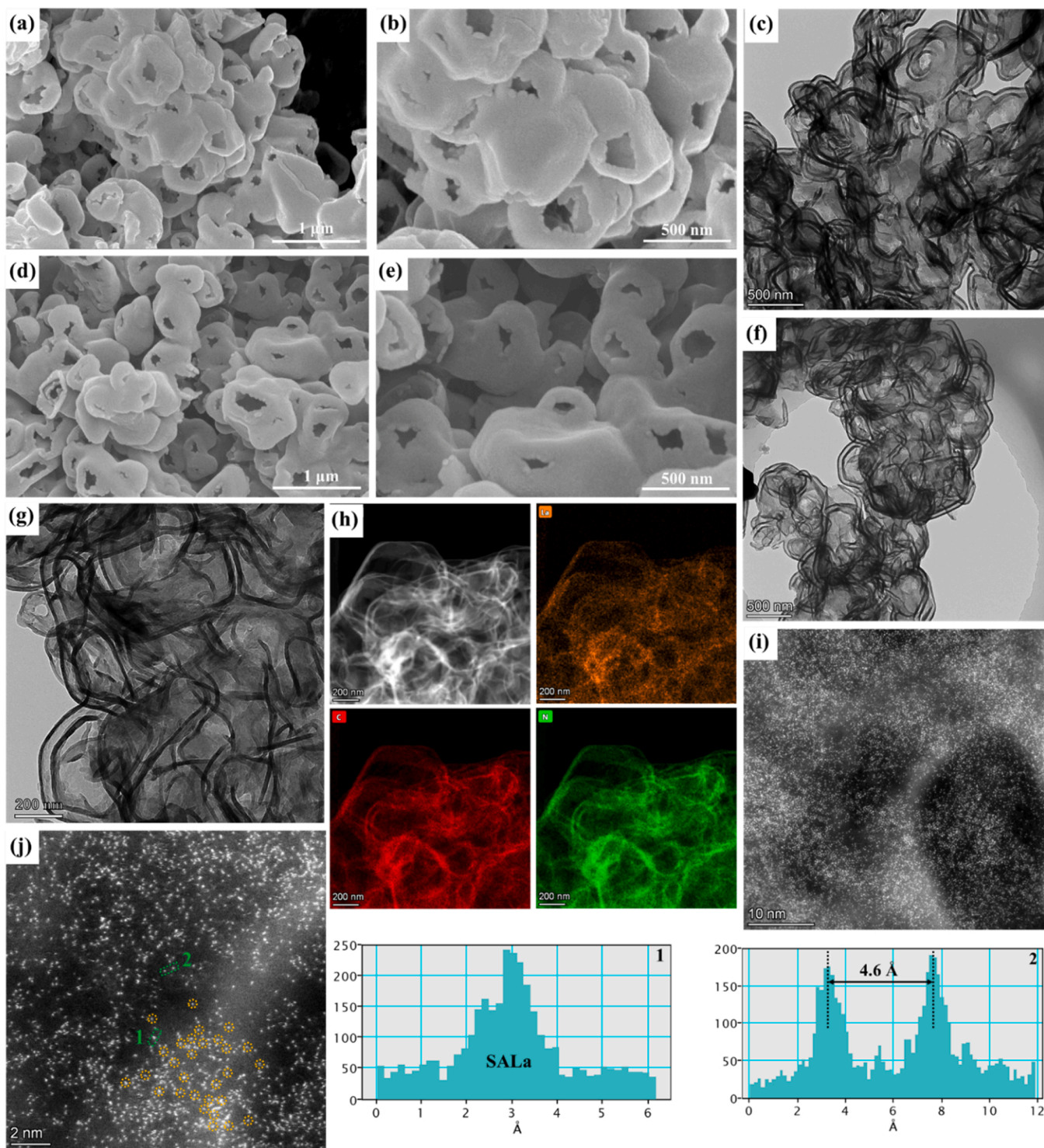


Fig. 1. (a, b) SEM images of 3DA-CN; (c) TEM image of 3DA-CN; (d, e) SEM images of SALa/CN; (f, g) TEM images of SALa/CN; (h) TEM with elemental mapping of SALa/CN; (i, j) AC-HAADF-STEM of SALa/CN.

foundation for the subsequent excellent photocatalytic activity.

3.2. Chemical state and structure analyses

To explore the chemical state of the as-prepared photocatalysts, X-ray photoelectron spectroscopy (XPS) was applied as a characterization technique and the results are shown in Fig. 2. An obvious new peak (marked in shadow) is observed in the full survey spectra of SALa/CN (Fig. 2a) compared with the survey spectra of 3DA-CN, which

demonstrates the coexistence of La, C and N elements. It indicates that La element was successfully introduced into 3DA-CN corresponding with the mapping results. The high-resolution La 3d spectra are revealed in Fig. 2b. The La 3d of La_2O_3 can be fitted into four peaks appearing at 834.9 eV, 838.6 eV, 851.8 eV and 855.4 eV, which correspond to La $3d_{5/2}$ and La $3d_{3/2}$. Interestingly, the La 3d peaks position of SALa/CN are shifted by 0.6 eV and toward the higher binding energy than the peak of La_2O_3 , indicating that the electronic orbital state of SALa is different from that of La (III) in La_2O_3 . That is, the coordination

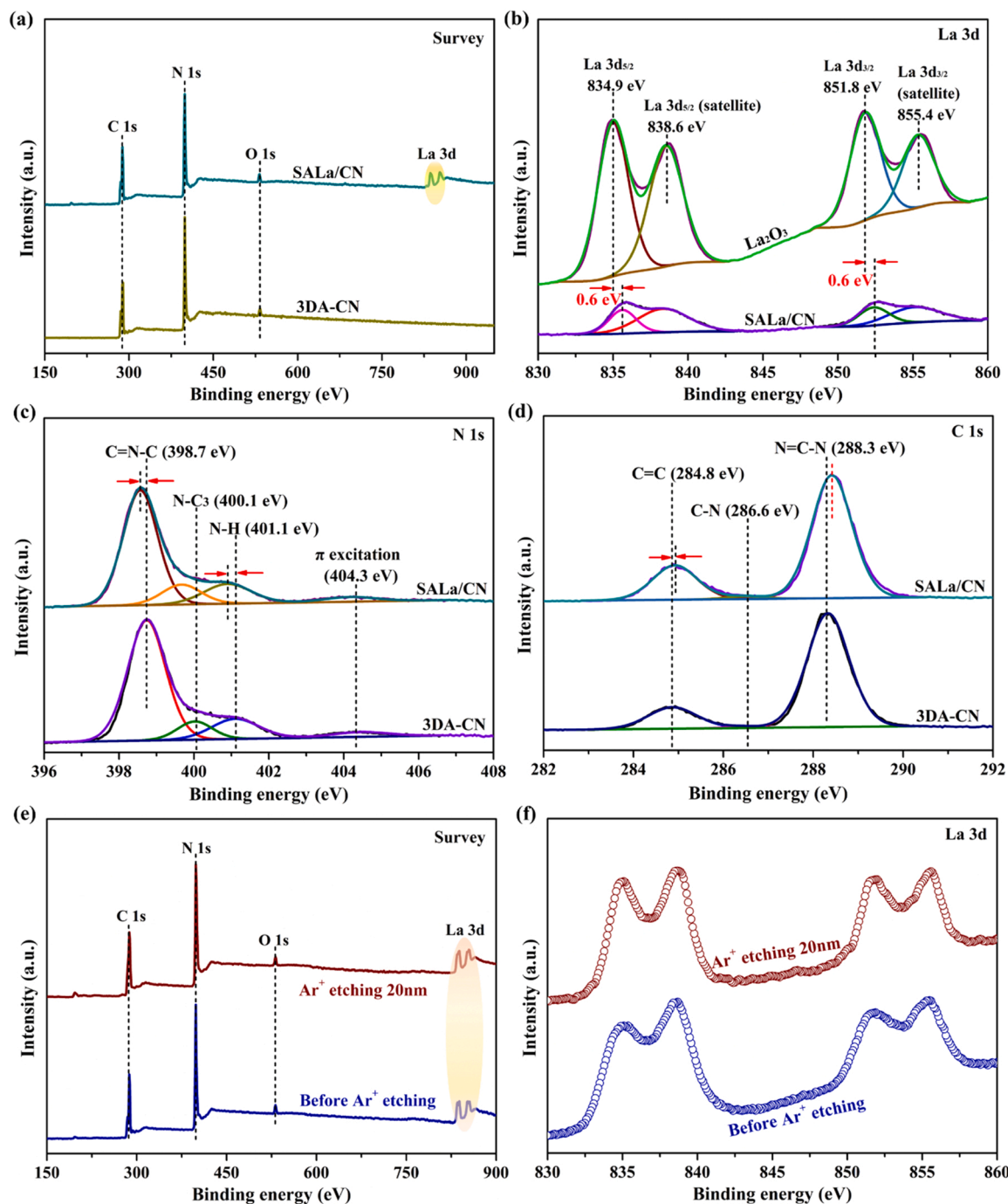


Fig. 2. (a) The XPS full survey spectra of 3DA-CN and SALa/CN; (b) La 3d of La_2O_3 and SALa/CN; (c) N 1 s and (d) C 1 s of 3DA-CN and SALa/CN; (e) the XPS full survey spectra and (f) La 3d of initial sample and Ar^+ etching 20 nm.

environment of La in SALa/CN is different from that of La (III). The specific coordination environment for SALa is illustrated later using X-ray absorption spectroscopy (XAS). Simultaneously, the N 1 s spectrum of 3DA-CN (Fig. 2c) exhibits four peaks, which are attributed to the C=N-C, N-C₃, N-H and π excitation positions at 398.7 eV, 400.1 eV, 401.1 eV and 404.3 eV, respectively. The N species of SALa/CN move to a lower binding energy direction relative to 3DA-CN. It suggests that there is a strong interaction between the SALa and 3DA-CN skeletons causing electrons to be transferred between them [15]. As depicted in Fig. 2d, three obvious peaks are located at 284.8 eV, 286.6 eV and 288.3 eV in the C 1 s spectrum of 3DA-CN, which are indexed to C=C, C-N and N = C-N bonds, respectively. The peak shape of C 1 s spectrum

also underwent a certain degree of change after the introduction of SALa, indicating an interaction between SALa and C atoms [37,38]. Therefore, SALa is successfully integrated into 3DA-CN and changes the electron cloud density of 3DA-CN. The distribution fitting of the O 1 s is presented in Fig. S1. The peak at 532.1 eV is attributed to the adsorption of H_2O from the environment on the material surface [39]. According to the survey spectrum analysis (Table S2), the mass ratio of SALa is 10.47 wt%. The consistent results of ICP-OES and XPS prove that SALa are not distributed on the catalyst surface. Meanwhile, the XPS argon ion etching experiment was implemented to further verify that the SALa is not distributed on the surface of 3DA-CN. As shown in Fig. 2e-f, argon ion etching at 20 nm still detected the characteristic peaks of La 3d with

the same intensity as the initial value and the corresponding analysis data (Table S3) suggest that the amount of La barely changed.

The X-ray absorption near-edge structure (XANES) and extended X-ray absorption fine structure (EXAFS) were performed to elucidate the electronic structure and coordination environment of SALa/CN. From the La L_3 -edge XANES spectra in Fig. 3a, the white line intensity of SALa/CN is higher than that of La_2O_3 , indicating that the average valence state of SALa is greater than +3 [40,41]. The valence state of SALa was also calculated as +3.29 by DFT calculations, which is consistent with the XANES results. The Fourier transformed (FT) k^3 -weight EXAFS spectra at the La L_3 -edge are applied to analyze the coordination environment of SALa (Fig. 3b). The FT-EXAFS spectrum of La_2O_3 was detected with a distinct peak at 2.08 Å, corresponding to La-O scattering. The peak of SALa/CN is located at 1.97 Å, which does not match the scattering path of La-O. The experimental value of La foil cannot be supplied because the chemical properties of lanthanum are too reactive. Therefore, the La foil was calculated using FEFF and the relevant calculation parameters are provided in the SI (Section 3). As a comparison, the La-La contribution is located at 3.23 Å in the La foil reference indicating the nonexistence of La-La in SALa/CN. Furthermore, a least-squares FT-EXAFS curve fitting of SALa/CN was obtained in Fig. 3c. The specific fitting parameters are presented in Table S4. The

results show that SALa coordinates with six N/C atoms on 3DA-CN. The corresponding EXAFS curves fitting in q -space and k -space are presented in Fig. S2. Subsequently, the possible models (Fig. S3-S4) were constructed by DFT calculations and the corresponding bond lengths are displayed in the diagram. It is deduced that the structure of SALa/CN is DLaN_4C_2 (double-layer coordination: four nitrogen and two carbon) according to the average coordination bond length (2.63 Å, Table S4). Therefore, a reasonable structural model is derived and embedded in Fig. 3c. We further calculated La L_3 -edge XANES spectra for SALa/CN theoretically implemented in FDMNES software, confirming that the theoretical spectrum of DLaN_4C_2 is consistent with the experimental data (Fig. 3d). Moreover, the first coordination shell of SALa/CN is located between La-C and La-N in Fig. 3e, which is consistent with the results of the above reasoning model. EXAFS calculation results by FEFF of different coordination environments of SALa samples (Fig. 3f) show obvious characteristic peaks of higher shells. The other low intensity peaks in SALa/CN may be caused by higher shells or noise and do not correspond to the peak of La_2O_3 [25,42]. According to the above analysis, the FT-EXAFS spectra further ruled out the presence of metallic La or La_2O_3 in the SALa/CN catalyst.

The in situ diffuse reflectance infrared Fourier transform spectroscopy (DRIFTS) of CO adsorption is a powerful technique to distinguish

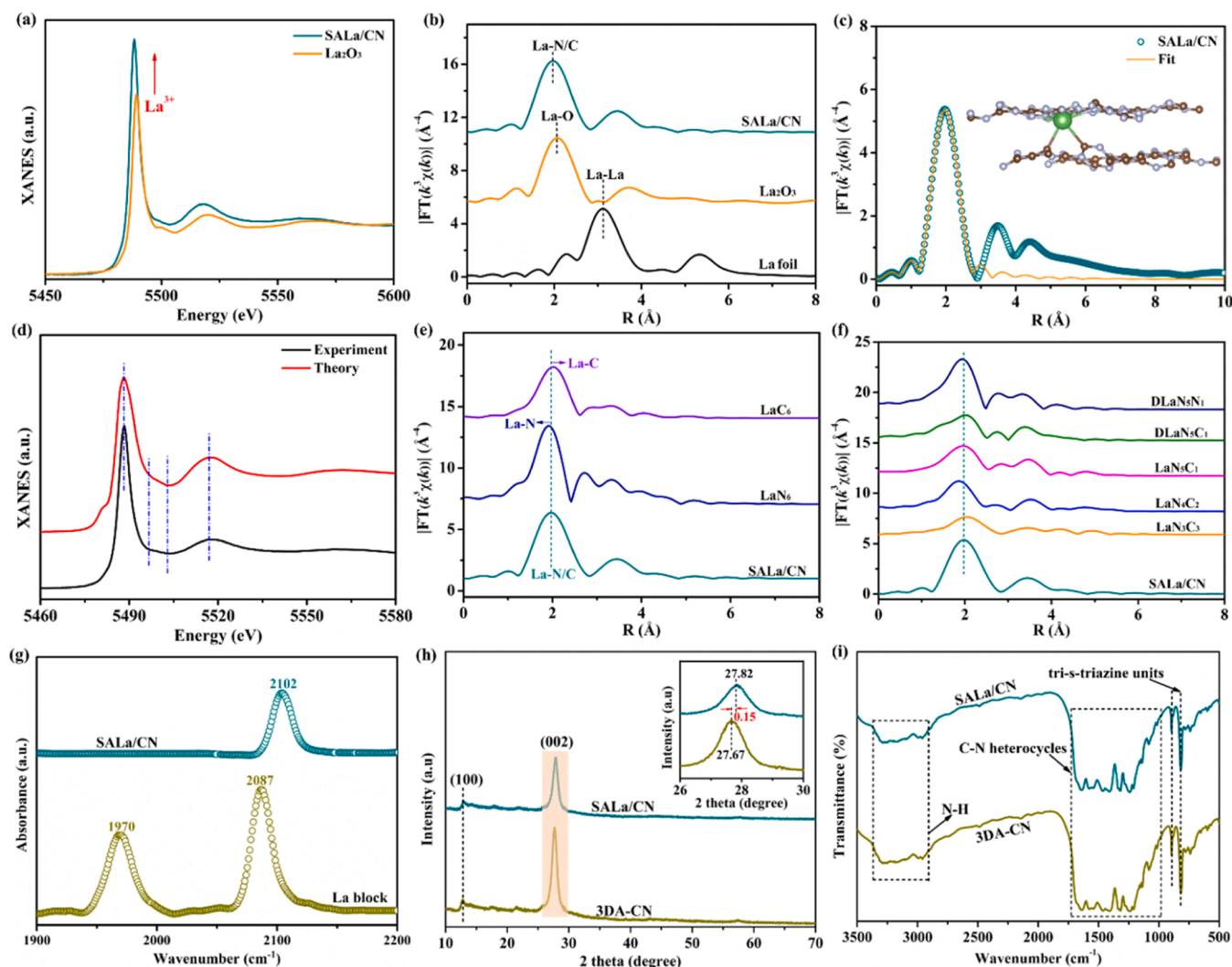


Fig. 3. (a) The normalized XANES spectra at the La L_3 edge of SALa/CN and La_2O_3 ; (b) the FT k^3 -weight EXAFS spectra of La foil, La_2O_3 and SALa/CN; (c) EXAFS fitting curve of SALa/CN; (d) Comparison between the experimental XANES spectrum of SALa/CN and theoretical spectrum of DLaN_4C_2 ; (e, f) FEFF calculation results of different coordination environments of SALa samples; (g) in situ DRIFTS of CO adsorption spectra on the SALa/CN and La block; (h) the XRD patterns (inset an enlarged version) and (i) FT-IR spectra of 3DA-CN and SALa/CN.

the single atom and aggregated sites. As shown in Fig. 3g, two distinct characteristic peaks are detected in the La block at 2087 and 1970 cm^{-1} , which are attributed to linear and bridge adsorption of CO, respectively. For the SALa/CN sample, only one characteristic peak at 2102 cm^{-1} is detected, corresponding to the linear adsorption peak of CO by SALa, suggesting that La species is atomically dispersed on the 3DA-CN support [43,44]. The crystalline structures of 3DA-CN and SALa/CN were detected by X-ray diffraction (XRD) and the corresponding XRD patterns are shown in Fig. 3h. Two distinct diffraction peaks at approximately 12.83° and 27.67° are found in 3DA-CN indexed as the (100) plane and (002) plane, respectively [45,46]. Specifically, the structural packing of tri-s-triazine motifs causes the (100) plane of 3DA-CN, and the (002) plane is caused by the periodic superposition of the conjugated aromatic system. Two characteristic peaks of 3DA-CN are still detected in the SALa/CN photocatalyst, indicating that the introduction of SALa can not

introduce other La species. Significantly, the diffraction peak at the (002) plane of SALa/CN is obviously moved to a higher angle (from 27.67° to 27.82°) compared with 3DA-CN in the illustration of Fig. 3h. According to Bragg's law, the introduction of SALa decreases the layer spacing of 3DA-CN triggering the strong interaction between SALa and N (C) atoms [41,47]. Based on the decreased interlayer stacking distance together with La 3d XPS argon ion etching results, the introduced SALa locate the interlayer of 3DA-CN [48–50]. The changes in the functional groups of the photocatalysts were confirmed by Fourier transform infrared (FT-IR) spectra, and the corresponding results are presented in Fig. 3i. The signals at 810 cm^{-1} and 885 cm^{-1} are ascribed to the vibration mode of tri-s-triazine units in 3DA-CN [51,52]. To further clearly study the interaction between photocatalysts, the FT-IR spectra of as-prepared samples at 750–950 cm^{-1} are magnified in Fig. S5. The results show that the tri-s-triazine units in SALa/CN is migrated to a

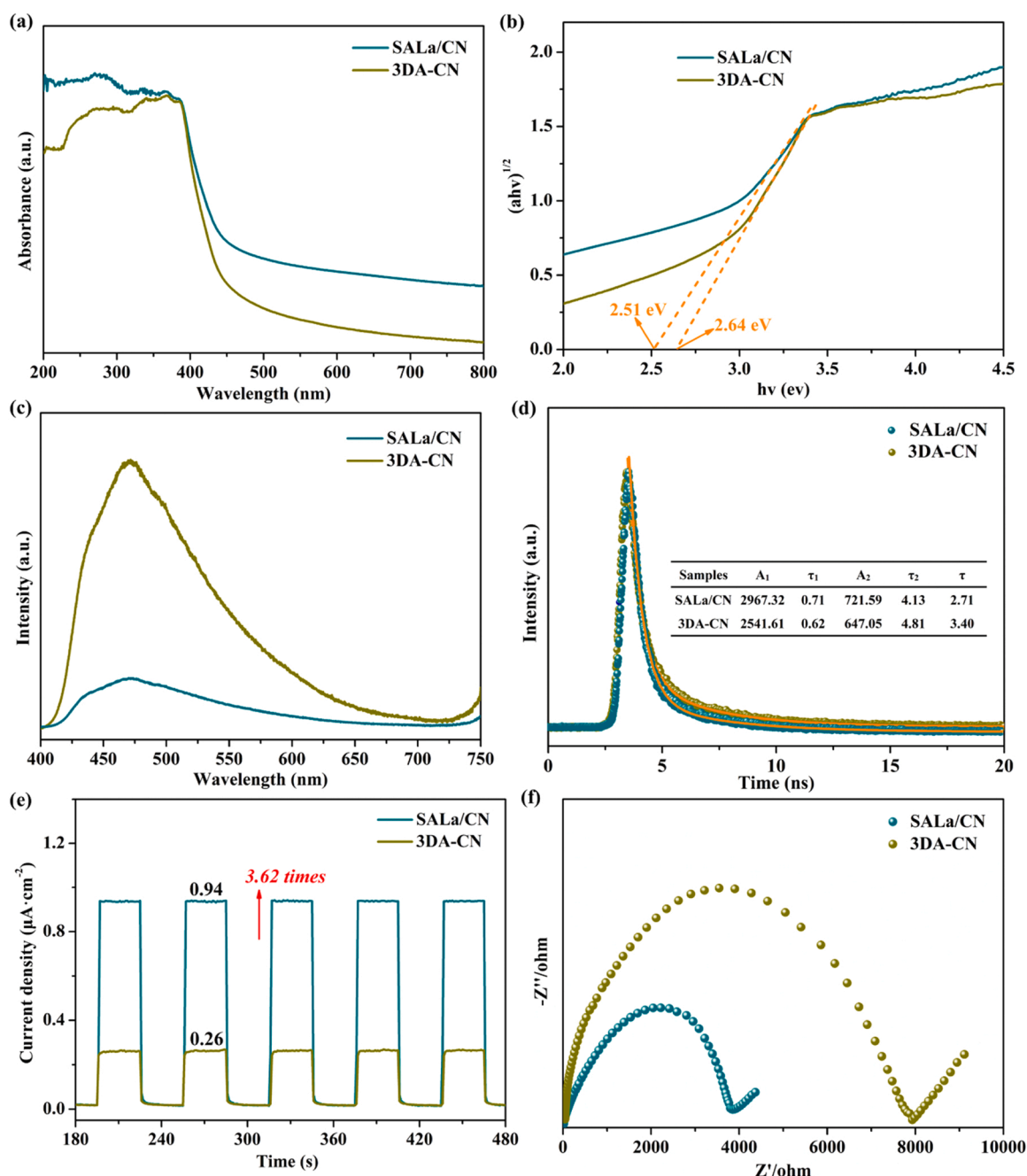


Fig. 4. (a) UV-vis DRS, (b) Tauc plots, (c) PL spectra, (d) TR-PL decay curves, (e) TPR and (f) Nyquist plots of 3DA-CN and SALa/CN.

higher wavenumber, indicating that SALa has been successfully introduced into the structure of 3DA-CN. The several vibration peaks at 980–1730 cm^{-1} are assigned to the C-N heterocycle, indicating the existence of a polymeric melon network for the as-prepared materials [53, 54]. The region for 3040–3370 cm^{-1} has obvious characteristic peaks, which are mainly caused by the stretching vibration of the N-H functional groups of 3DA-CN.

3.3. Optical and photoelectrochemical properties

The light absorption properties of 3DA-CN and SALa/CN were characterized by UV–vis diffuse reflectance spectrometry (UV–vis DRS). As shown in Fig. 4a, 3DA-CN exhibits an inherent absorption peak at approximately 460 nm. An obvious red-shift is found in the absorption edge of SALa/CN compared with 3DA-CN. It indicates that the incorporation of SALa into the 3DA-CN lattice broadens the optical absorption ability. More importantly, the absorption peak of SALa/CN in the visible region is significantly enhanced. Therefore, the introduction of SALa improves the light utilization efficiency and provides the possibility for excellent properties of materials. The bandgaps of 3DA-CN and SALa/CN are plotted by the Kubelka–Munk theory in Fig. 4b. The bandgap (E_g) of SALa/CN (2.51 eV) is narrower than that of 3DA-CN (2.64 eV), meaning that SALa/CN needs lower energy to be excited in the process of the photocatalytic reaction [55].

Moreover, the optical parameters of the as-prepared photocatalysts in aqueous suspension were analyzed. The absorbances of 3DA-CN and SALa/CN are shown in Fig. S6. According to the Beer–Lambert law (Eq. (1)), the absorption coefficient (ϵ) is obtained.

$$A = -\lg\left(\frac{I}{I_0}\right) = \lg T = \epsilon bc \quad (1)$$

where, A , I , I_0 , T , b and c represent absorbance, transmitted light intensity, incident light intensity, transmittance, absorption layer thickness and concentration of light absorbing substance, respectively. The specific absorption coefficients (ϵ^*) of 3DA-CN and SALa/CN are 875 and 2125 cm^2/g , respectively. The extinction coefficient (β) of the catalysts is calculated from the transmittance value using Eq. (2) and L_{cell} is the cell path length (m). The average extinction coefficients (β^*) of 3DA-CN and SALa/CN obtained by performing linear regression over β are calculated to be 7250 and 14,500 cm^2/g , respectively. The relationship among the scattering coefficient (α^*), ϵ^* and β^* are presented in Eq. (3). The values of optical parameters are shown in Table S5.

$$\beta = 2.303 \left(-\frac{\lg T}{L_{\text{cell}}} \right) \quad (2)$$

$$\alpha^* = \beta^* - \epsilon^* \quad (3)$$

$$\delta = h \times C \times \epsilon^* \quad (4)$$

The optical thickness (δ) of 3DA-CN and SALa/CN is obtained in Eq. (4) (h : the height of liquid in the photocatalytic reaction system; C : the concentration of the photocatalyst). Therefore, the δ results for 3DA-CN and SALa/CN are 2.12 and 3.97, respectively. The δ values of 3DA-CN and SALa/CN conform to the optimum range of δ (1.8–4.4) in the photocatalytic system [56,57]. Moreover, the ϵ^* of SALa/CN is larger than that of 3DA-CN, which means that the introduction of SALa enhances the photocatalytic activity of the catalyst.

The effective separation of electrons and holes generated after semiconductor excitation is the key factor in improving material properties. Thus, the photoluminescence (PL) spectra of 3DA-CN and SALa/CN are analyzed in Fig. 4c. Compared with 3DA-CN, the addition of SALa significantly reduces the PL peak intensity of SALa/CN. It demonstrates that SALa/CN has excellent carriers separation efficiency. The position of the strongest emission wavelength (470 nm) of SALa/CN is slightly offset, which is caused by mutual electrons transfer to SALa and

3DA-CN [58,59]. Moreover, the lifetimes of photogenerated carriers are obtained by time-resolved photoluminescence (TR-PL) spectra in Fig. 4d. The spectra are analyzed by the double-exponential method using Eq. (5).

$$R(t) = A_1 \exp\left(-\frac{t}{\tau_1}\right) + A_2 \exp\left(-\frac{t}{\tau_2}\right) \quad (5)$$

where, A_1 , A_2 , τ_1 and τ_2 are separately defined as the amplitude of the normalized decay ingredient and lifetime values. The average lifetime (τ_{ave}) values are calculated by Eq. (6).

$$\tau_{\text{ave}} = \frac{A_1 \tau_1^2 + A_2 \tau_2^2}{A_1 \tau_1 + A_2 \tau_2} \quad (6)$$

As shown in the inlaid table of Fig. 4d, the carriers lifetime of SALa/CN is lower than that of 3DA-CN, indicating that the carriers can be effectively separated after the introduction of SALa [60,61]. The decrease in lifetime indicates that the main form of electrons transition is nonradiative transition and that electrons mainly participate in the photocatalytic reaction. Instead, electrons are returned to the ground state in the form of emitted photons and used to emit light in the excited state as radiation [62].

Transient photocurrent response (TPR) and electrochemical impedance spectroscopy (EIS) are significant characterization methods for the photoelectrochemical properties of materials. As depicted in Fig. 4e, the photocurrent intensity of SALa/CN ($0.94 \mu\text{A}\cdot\text{cm}^{-2}$) is significantly increased about 3.62 times that of 3DA-CN ($0.26 \mu\text{A}\cdot\text{cm}^{-2}$), indicating that the introduction of SALa obviously promotes the separation of electrons and holes [63,64]. Moreover, the Nyquist curves of 3DA-CN and SALa/CN are exhibited in Fig. 4f. It is well known that the smaller radius of EIS means the higher separation efficiency of carriers; consequently, SALa/CN has better charge separation efficiency than 3DA-CN [65,66]. Namely, SALa/CN has an excellent light utilization rate, high visible light absorption capacity and efficient carriers separation efficiency. Moreover, the specific surface area is an important factor affecting the photocatalytic activity of catalysts. Thus, N_2 adsorption/desorption isotherm experiments were applied to measure the specific surface of 3DA-CN and SALa/CN. As shown in Fig. S7, the curves of the as-prepared samples clarify the typical IV isotherm with H_3 hysteresis loops, indicating that the pore structure of the materials is conducive to increasing the contact time with pollutants. SALa/CN ($97.059 \text{ m}^2/\text{g}$) has larger specific surface area than 3DA-CN ($92.478 \text{ m}^2/\text{g}$), indicating that the introduction of SALa provides more active sites for the reaction leading to higher degradation rates [67,68]. The specific surface area details of 3DA-CN and SALa/CN are summarized in Table S6.

3.4. Density functional theory (DFT) calculations

To investigate the advantages of SALa/CN catalyst with DLaN_4C_2 configuration, we studied the influence of SALa/CN and 3DA-CN on O_2 selectivity by DFT calculations and the optimized configurations of O_2 adsorption are presented in Fig. 5a–b. The computational details are presented in the SI (Section 4). The corresponding O_2 adsorption energy (E_{ads}) data are presented next to the corresponding configurations. The E_{ads} for 3DA-CN and DLaN_4C_2 models are -0.102 eV and -0.504 eV , respectively. Moreover, superoxide free radical ($\bullet\text{O}_2^-$) plays major active specie in the photocatalytic reaction of this experimental system, and the corresponding investigations are presented in later capture experiments and ESR tests. Therefore, the feasibility of generating $\bullet\text{O}_2^-$ by O_2 adsorption on the as-prepared catalysts is discussed in Fig. 5c. Gibbs free energy (G) is a function of chemical thermodynamics used to determine the direction of process. The G could be calculated according to the same method as in the literature [69], in which G is calculated by Eqs. (7–8).

$$G_{\text{gas}} = H - TS = E_{\text{ele}} + \text{ZPE} + RT - TS \quad (7)$$

$$G_{\text{solid}} = H - TS = E_{\text{ele}} + \text{ZPE} - TS \quad (8)$$

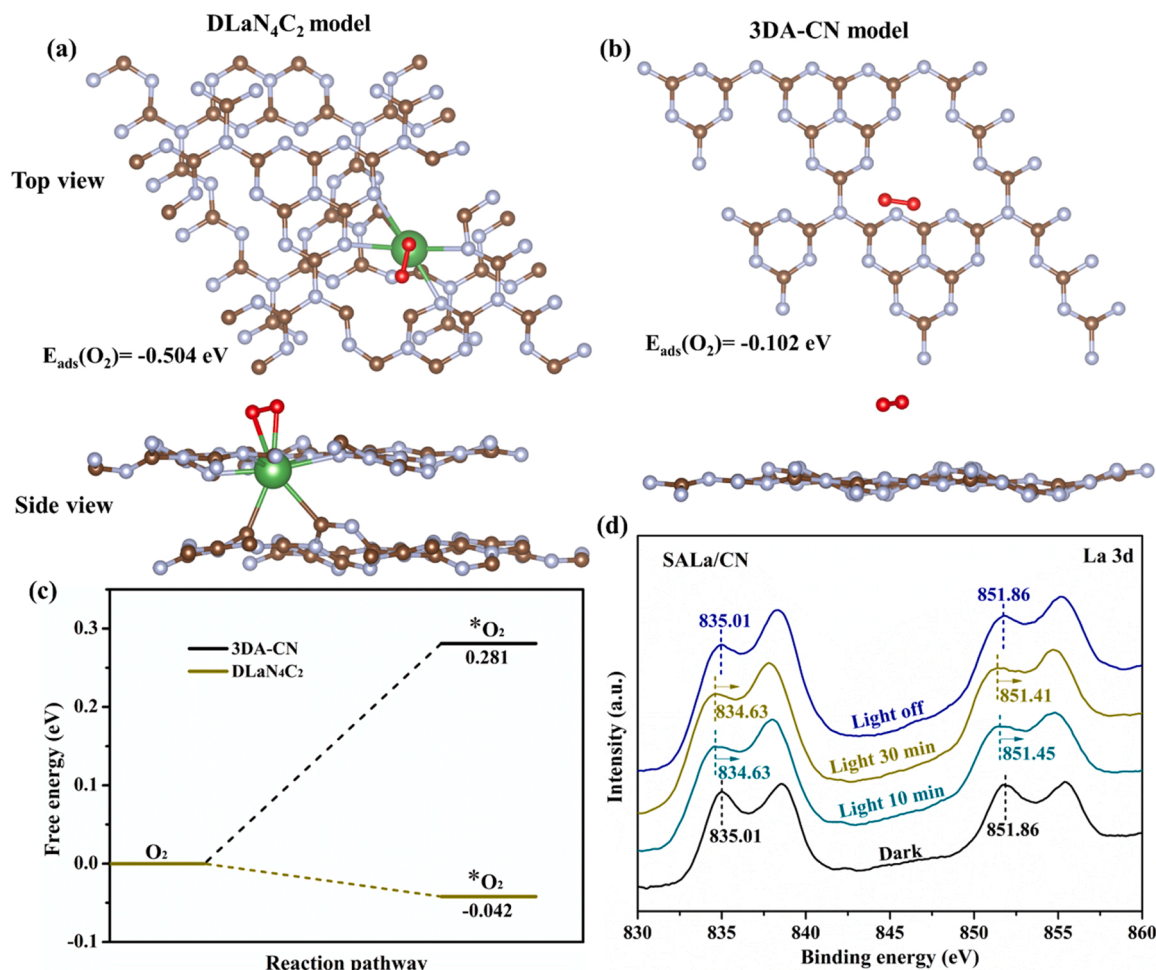


Fig. 5. The optimized models of O₂ adsorption for (a) DLaN₄C₂ and (b) 3DA-CN; (c) the G of 3DA-CN and DLaN₄C₂ for the production of •O₂⁻ and (d) La 3d XPS spectra of SALa/CN in the dark or light.

where H , T , S , E_{ele} and ZPE represent the enthalpy, Kelvin temperature, entropy, ground-state electronic energy of the structure and zero-point energy, respectively. R is the gas constant (8.62×10^{-5} eV/(mol·eK)). Obviously, the DLaN₄C₂ (-0.042 eV) configuration is more likely to generate superoxide radical (•O₂⁻) than 3DA-CN (0.281 eV) from a thermodynamic perspective. It indicates that the as-prepared single atom catalyst (DLaN₄C₂) has better ability to activate O₂ and more efficient selectivity for the generation of •O₂⁻ than 3DA-CN. In addition, the XPS of SALa/CN under light irradiation condition was studied. As shown in Fig. 5d, the XPS peak of La 3d obviously are moved the direction of low binding energy under light irradiation, which means that SALa acts as an electron acceptor. SALa serves as the O₂ reduction sites in the process of photocatalytic reaction and O₂ is converted to •O₂⁻ acting on pollutant molecules [70]. The peak of La is returned to its original state when the light source is turned off. More importantly, SALa can be used as a bridge to transfer electrons from the catalyst support to O₂, thus achieving efficient photocatalytic activity [71,72]. The main reason for the high activity of SACs is the coordination between the metal single-atom and the surrounding atoms.

The electrostatic potential (ESP) and electronic localization function (ELF) are used to research the microelectronic structure of as-prepared materials. As shown in Fig. S8, there are lone pair electrons on the pyridine nitrogen of 3DA-CN promoting single metal atom to form coordination bond with N atoms. The surface electrostatic potential of SALa/CN is controlled by a negative electrostatic potential in Fig. 6a, which may result in the transfer of electrons from SALa to 3DA-CN. The ELF of SALa/CN (Fig. 6b) indicates that SALa strongly interacts with N

and C atoms. The electron localization of the ELF in the path of La-N (La and four adjacent N atoms) and La-C (La and two C atoms in other layer) has high values, which confirms that there are covalent bonds between La-N and La-C [73,74]. Moreover, the direction of electrons transfer after the introduction of SALa is studied by electron density difference (EDD). As shown in Fig. 6c, the electron cloud density between N or C atoms for 3DA-CN and SALa is relatively enriched in the spatial direction, which makes the electron migration ability higher than that of pure 3DA-CN and thus improves the separation efficiency of charge [75]. The density of states (DOS) of 3DA-CN reveals that the valence band maximum (VBM) contributes to the p orbitals of N (N(p)) and C (C(p)) in Fig. 6d, which corresponds with previous reports [76]. The VBM of SALa/CN (Fig. 6e) is mainly contributed by N(p) and C(p), indicating that there are significant local electrons of N and C atoms around the SALa. Additionally, the d contribution of La (La(d)) and the C(p) contribution closely overlap, illustrating the existence of p – d orbital hybridization between SALa and C atoms. The conduction band minimum (CBM) overlaps highly with the C(p) and N(p), indicating that SALa/CN also exhibits the orbital hybridization in the CBM. The work functions (Φ) of 3DA-CN and SALa/CN are investigated in Fig. 6f-g, which represents the minimum energy required for electrons to escape immediately from the surface of the catalyst [77,78]. The calculated Φ of 3DA-CN is 5.65 eV and the Φ of SALa/CN decreases to 4.21 eV. SALa/CN requires the lower energy to enable electrons escape, allowing higher concentrations of photogenerated electrons to be produced.

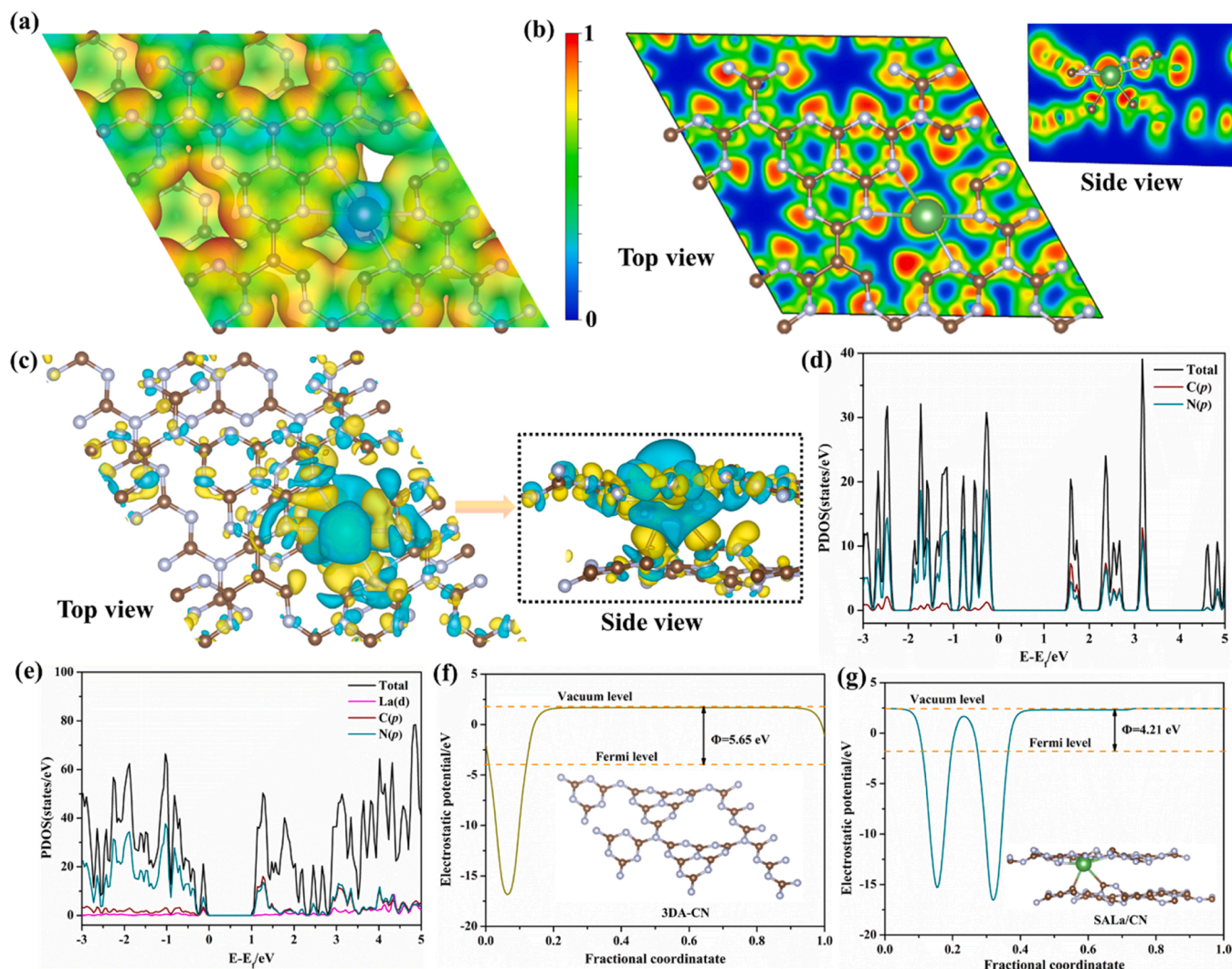


Fig. 6. (a) ESP of SALa/CN with an isosurface of 0.02 e/Bohr^3 ; (b) ELF of SALa/CN and (c) EDD of SALa/CN with an isosurface of 0.002 e/Å^3 ; (d, e) The DOS of 3DA-CN and SALa/CN; (f, g) work function of 3DA-CN and SALa/CN by DFT calculations.

3.5. Photocatalytic activity tests

3.5.1. Photocatalytic degradation of antibiotic experiments

To detect the synergistic effect of the improved strategy, the photocatalytic degradation of TC (20 mg/L, 100 mL) was carried out under simulated sunlight ($\lambda > 420 \text{ nm}$). The specific experimental implementation process has been mentioned in Section 2.4. The degradation efficiency (DE) can be calculated by Eq. (9) for the concentration of TC in the solution for t minutes (C_t) and the initial concentration of TC (C_0).

$$DE(\%) = \left(1 - \frac{C_t}{C_0}\right) \times 100\% \quad (9)$$

As shown in Fig. 7a, the photocatalytic activity of SALa/CN (98.38%) is significantly increased compared with that of 3DA-CN (31.90%). Meanwhile, the TC removal activity of SALa/CN is better than that of most $g\text{-C}_3\text{N}_4$ -based photocatalysts compared with previous reported studies (Table S7). The introduction of SALa realizes the effective separation of electrons and holes in space and enhances the utilization rate of visible light. Moreover, SALa provides a new site for O_2 activation and special coordination structure, which makes the as-prepared material highly selective to O_2 , so that more active species ($\bullet\text{O}_2^-$) can act on pollutant molecules and thus efficiently remove pollutants. The corresponding kinetic constants (k), fitted by a first-order kinetic model, for quantitative comparison are depicted in Fig. 7b. SALa/CN exhibits the

larger slope than 3DA-CN, meaning that it has excellent photocatalytic activity relative to 3DA-CN. The k values of 3DA-CN and SALa/CN are presented in the illustration of Fig. 7b. The k value of SALa/CN (0.10661 min^{-1}) achieves 9.81 times than that of 3DA-CN (0.01087 min^{-1}). Therefore, the introduction of SALa is an effective strategy to improve photocatalyst activity. Total organic carbon (TOC) characterization was applied to evaluate the mineralization performance of the SALa/CN photocatalytic system for TC. As shown in Fig. S9, the SALa/CN displays the excellent removal rate (73.27%) in 30 min implying that SALa/CN has fantabulous mineralization activity for TC. The high rate of mineralization means that SALa/CN has the ability to convert TC into small pollutant-free molecules (CO_2 , H_2O , etc.) [79,80]. To study the applicability of SALa/CN for the removal of other antibiotics, photocatalytic degradation experiments of oxytetracycline hydrochloride (OTC) and doxycycline hydrochloride (DOX) were performed. As shown in Fig. 7c, the degradation efficiency of OTC and DOX by the SALa/CN photocatalyst reached 84.49% and 91.71% within 30 min, respectively. It indicates that SALa/CN has generally excellent photocatalytic activity for the removal of antibiotics. Moreover, we simulated the degradation of TC by SALa/CN in the real environment with water from Xuanwu Lake in Nanjing and tap water from the laboratory. In real water environment, SALa/CN material still shows fantabulous photocatalytic performance in Fig. 7d, with degradation rates of 92.51% and 94.66% in lake water and tap water, respectively.

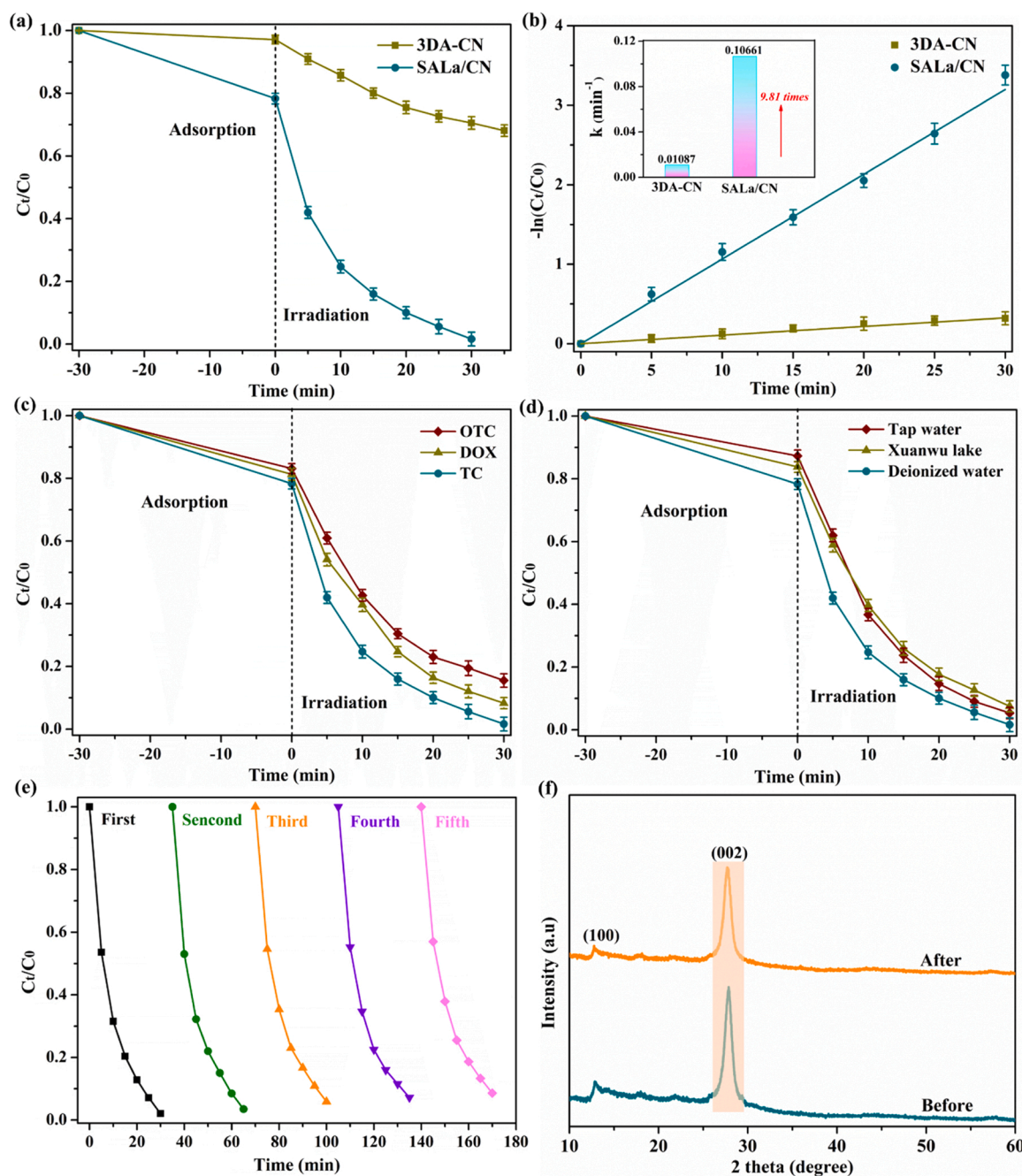


Fig. 7. (a) Time-concentration plots; (b) pseudo-first-order kinetic curves (inset apparent reaction rate constant k) for photocatalytic degradation of TC; (c) photocatalytic degradation of different organic pollutants, (d) real water environment degradation and (e) cycle degradation experiments of SALa/CN; (f) XRD patterns of SALa/CN before and after cycle experiments.

From what has been discussed above, SALa/CN has high efficiency and practical application value in treating sewage antibiotics.

The reusability and durability of photocatalysts is an important factor in evaluating the practical application of photocatalysts. Five cycles were used to evaluate the indicator and the results are shown in Fig. 7e. The SALa/CN photocatalyst still has good photocatalytic activity after five cycles and the degradation efficiency is decreased slightly, which might be due to a certain amount lost in the process of collecting the catalyst after the cycle experiments. To study whether the morphology and crystal structure of SALa/CN changed after the cyclic experiment, AC-HAADF-STEM and XRD were performed. As depicted in Fig. S10, the AC-HAADF-STEM result of SALa/CN after the cycling experiment still presents scattered single atoms, and no agglomeration

clusters or particles are found, which reveals that SALa embedded in 3DA-CN is stable in the photocatalytic process. Moreover, SALa/CN was detected with the same crystal structure as before the reaction in Fig. 7f. The above experiments and characterizations prove that SALa/CN has excellent reusability and durability and possesses certain potential in practical applications.

3.6. Mechanism investigations

It is essential to explore the active species in which photocatalytic systems operate. Therefore, active species trapping experiments were applied to study the mechanism for the degradation of TC by SALa/CN. Specifically, ascorbic acid (AA), ethylenediaminetetraacetic acid

disodium (EDTA-2Na), L-tryptophan, catalase (CAT) and isopropanol (IPA) are used as trapping agents to capture superoxide radical ($\bullet\text{O}_2^-$), holes (h^+), singlet oxygen ($^1\text{O}_2$), hydrogen peroxide (H_2O_2) and hydroxyl radical ($\bullet\text{OH}$), respectively [21,81,82]. As clarified in Fig. 8a, the degradation activity of SALa/CN (22.67%) is substantially suppressed after the addition of AA, which indicates that $\bullet\text{O}_2^-$ is the dominant active species in the photocatalytic reaction process. The addition of L-tryptophan makes the degradation efficiency of TC by SALa/CN only 31.02%, indicating that $^1\text{O}_2$ is also one of the decisive active species involved in the photocatalytic degradation reaction. In contrast, the photocatalytic degradation efficiency of TC (89.04%) is hardly decreased by combining with IPA, illustrating that $\bullet\text{OH}$ plays a minor role in the degradation process. Moreover, the TC degradation efficiency decreased to 40.74% when the h^+ was captured by EDTA-2Na. The

degradation efficiency of SALa/CN shows a downward trend (70.91%) after capturing H_2O_2 by CAT. Hence, it is obvious that the contribution degree of active species is in the order of $\bullet\text{O}_2^- > ^1\text{O}_2 > \text{h}^+ > \text{H}_2\text{O}_2 > \bullet\text{OH}$.

To further declare the presence of free radicals in the degradation system of SALa/CN, the electron spin resonance (ESR) tests were performed and the corresponding results are shown in Fig. 8b-d. 5,5-dimethyl-1-pyrroline-N-oxide (DMPO), 2,2,6,6-tetramethyl-4-piperidone (TEMP) and 2,2,6,6-tetramethyl-1-piperidinyloxy (TEMPO) were used as capture agents to separately capture $\bullet\text{O}_2^-$, $^1\text{O}_2$ and h^+ . As depicted in Fig. 8b, the characteristic peak of DMPO- $\bullet\text{O}_2^-$ is not detected signal under darkness, although significant signal peaks are detected under visible light. SALa/CN exhibits the higher signal peak than 3DA-CN. It indicates that SALa effectively activates more oxygen (O_2) to

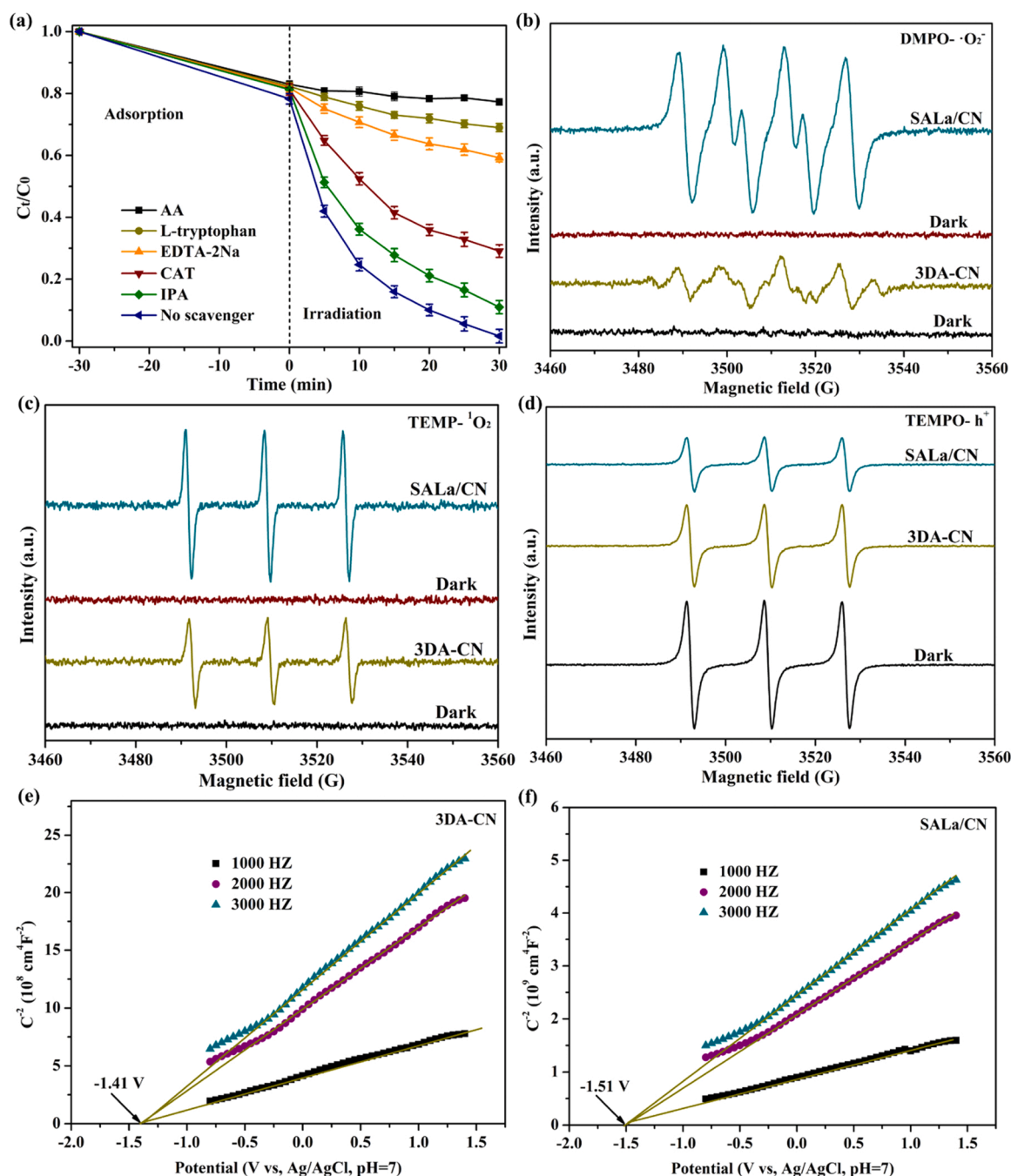


Fig. 8. (a) The trapping experiments of SALa/CN; (b-d) ESR spectra of the as-prepared photocatalysts; (e, f) Mott-Schottky plots of 3DA-CN and SALa/CN.

produce $\bullet\text{O}_2^-$ and thus SALa/CN has excellent photocatalytic performance [32,83]. In addition, the TEMP $^1\text{O}_2$ peak intensity of SALa/CN is obviously stronger than that of 3DA-CN, indicating that SALa is beneficial to the production of more $^1\text{O}_2$ and thus $^1\text{O}_2$ is used to break down pollutant molecules [84]. The relative peak magnitude is 1:1:1 (Fig. 8d) corresponding to TEMPO $\sim h^+$. The signal peaks are detected in the dark, due to the presence of a single electron in the capture reagent (TEMPO). Noticeably, the signal peaks are decreased under visible light irradiation, signifying that the as-prepared materials can generate h^+ to neutralize the lone pair electrons of TEMPO [85]. Moreover, the introduction of SALa promotes the generation of h^+ , which means that SALa/CN can produce more h^+ to act on pollutant molecules in the process of photocatalytic treatment for antibiotics. Therefore, $\bullet\text{O}_2^-$, $^1\text{O}_2$

and h^+ are the main active substances in this photocatalytic process, which is consistent with the results of the capture experiments.

To investigate the valence band (VB) and conduction band (CB) positions of the as-prepared samples, Mott-Schottky (M-S) tests were conducted in Fig. 8e. The CB positions of 3DA-CN and SALa/CN are -1.21 V and -1.31 V, respectively. The position of the CB is obviously moved up, which facilitates the production of $\bullet\text{O}_2^-$. The E_g values of 3DA-CN (2.64 eV) and SALa/CN (2.51 eV) were obtained by the Kubelka-Munk theory in Fig. 4b. The introduction of SALa decreases the E_g of 3DA-CN promoting the light absorption. Therefore, the VB positions of the 3DA-CN (1.43 V) and SALa/CN (1.20 V) were obtained according to the formula $E_{\text{VB}} = E_{\text{CB}} + E_g$ [86]. To further verify the correctness of the CB and VB positions, VB-XPS spectra are applied to

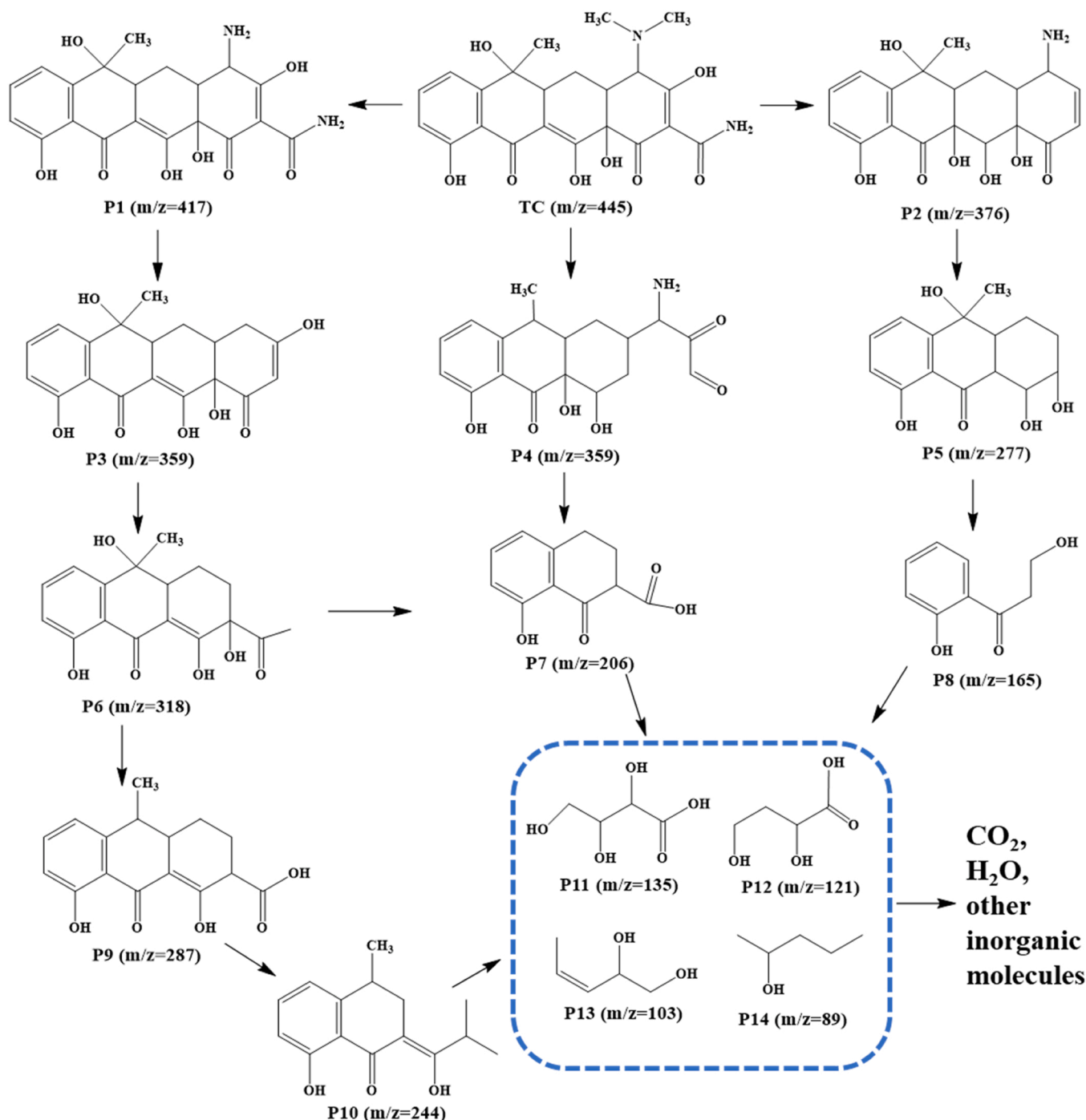


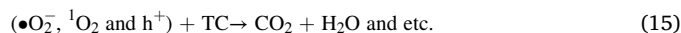
Fig. 9. The possible degradation pathway of TC molecule during the removal process.

deduce the VB positions. As illustrated in Fig. S11, the VB-XPS spectra detection positions of 3DA-CN and SALa/CN are 1.26 eV and 1.03 eV, respectively. The test data need to be converted according to the formula $E_{\text{NHE}}/V = 4.63 + f - 4.44$ (E_{NHE} : standard hydrogen electrode potential; f : sample VB test location) [46]. Therefore, the real E_{VB} of 3DA-CN and SALa/CN are 1.45 V and 1.22 V, respectively, which are consistent with those described above. The detailed band structure diagrams of 3DA-CN and SALa/CN are described in Fig. S12.

The possible degradation pathways and intermediates of TC were proposed by liquid chromatography–mass spectrometry (LC–MS). The LC–MS results of photocatalytic reaction for 0, 10, 20 and 30 min are shown in Fig. S13. It is evident that the photocatalytic reaction begins with a strong peak at $m/z = 445$, corresponding to the protonated TC molecule. New peaks are detected with the increasing reaction time, meaning that TC was broken down into other intermediates. Moreover, the peak of TC is decreased and almost disappeared at 30 min. The new signal peaks were found at 10 min, but disappeared or decreased at 20 min and 30 min. Moreover, some lower m/z signals were produced or significantly increased. It suggests that intermediates can be further destroyed and eventually broken down into CO_2 , H_2O and other small molecules. In combination with the LC–MS diagram results and relevant literatures, the possible TC degradation paths of SALa are presented in Fig. 9. Firstly, The TC was decomposed into P1 ($m/z = 417$) after demethylation via $\bullet\text{O}_2^-$ and $^1\text{O}_2$ oxidation processes [87]. P1 molecules undergo the elimination and deamidation reactions under the action of $\bullet\text{O}_2^-$ and h^+ to produce P3 ($m/z = 359$) [79]. P3 is fragmented to P6 ($m/z = 318$) by demethylation and ring-opening. Intermediate product P6 can be attacked by h^+ leading to the formation of product P9 ($m/z = 287$) by dehydration reaction. And P9 is further decomposed to P10 ($m/z = 244$) with the loss of carbonyl groups. Meanwhile, TC can be amidated to form P2 ($m/z = 376$) and is also demethylated and ring-opened to produce P4 ($m/z = 359$). Intermediate P7 ($m/z = 206$) can be generated by breaking the cyclic hydrocarbon structure of P4. P5 ($m/z = 277$) and P8 ($m/z = 165$) can be obtained from cyclic hydrocarbon structure fractures. The above intermediate products are further decomposed into ring-opening products (P11 ($m/z = 135$), P12 ($m/z = 121$), P13 ($m/z = 103$) and P14 ($m/z = 89$)) with the oxidation of the benzene ring structure. Eventually, these products are further mineralized into CO_2 , H_2O and other small molecules [88].

Through the above investigations, a possible mechanism of TC degradation is proposed (Fig. 10). The introduction of SALa improves the absorption capacity of the photocatalyst for visible light, and SALa/CN

CN requires lower energy to excite producing electrons and holes (Eq. (10)). The CB position of SALa/CN is located at -1.31 V vs normal hydrogen electrode (NHE), which is more negative than the redox potential of $\text{O}_2/\bullet\text{O}_2^-$ (-0.33 V vs NHE). The electrons are migrated from the VB of SALa/CN to the CB, where electrons combine with O_2 to form $\bullet\text{O}_2^-$ (Eq. (11)). Moreover, SALa acts as an active site enhancing the ability to activate O_2 and can be used as a bridge to transfer electrons from the catalyst support to the O_2 promoting charge transfer and separation. DLaN_4C_2 has a more negative G value resulting in the easier formation of $\bullet\text{O}_2^-$. The special bilayer coordination structure promotes the effective separation of charge in space, thus achieving efficient photocatalytic activity. Furthermore, $\bullet\text{O}_2^-$ can react with h^+ to generate $^1\text{O}_2$ (Eq. (12)) and react with H^+ to form H_2O_2 (Eq. (13)). The h^+ can directly react with H_2O in solution to form O_2 providing the raw material for the main reactive species (Eq. (14)) and can also act directly on pollutant molecules (Eq. (15)). The capture experiments and ESR tests clarified that $\bullet\text{O}_2^-$, $^1\text{O}_2$ and h^+ are the main active species to remove TC and convert TC into some pollution-free small molecules (Eq. (15)).



4. Conclusions

In summary, a high loading rare earth SALa bridge on 3DA-CN achieving the effective separation of charge in space has been designed for efficient photocatalytic activity. AC-HAADF-STEM, XANES and EXAFS elucidate that SALa has been successfully introduced into 3DA-CN, and that the coordination configuration with 3DA-CN is the DLaN_4C_2 configuration. DFT calculations suggest that the DLaN_4C_2 (-0.042 eV) configuration is more likely to generate $\bullet\text{O}_2^-$ than the 3DA-CN (0.281 eV) from a thermodynamic perspective. It means that the as-prepared single-atom catalyst has excellent ability to activate O_2 and more efficient selectivity for the generation of $\bullet\text{O}_2^-$. UV–vis DRS, PL, TR–

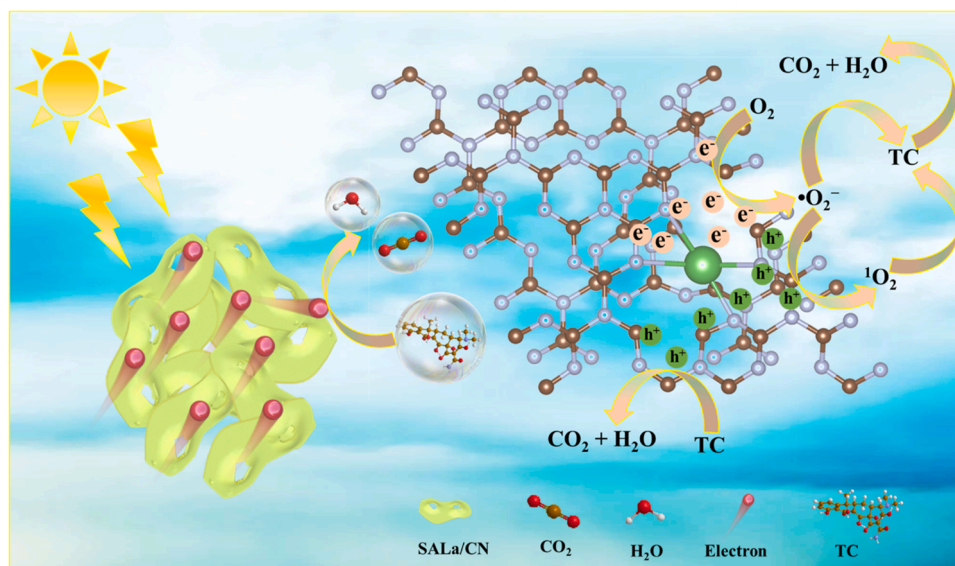


Fig. 10. The proposed photocatalytic degradation mechanism of SALa/CN for TC.

PL and electrochemical experiments have clarified that SALa/CN exhibits excellent visible light utilization and efficient carriers separation efficiency. SALa/CN shows excellent antibiotic degradation activity, and the degradation rates of TC, OTC and DOX are 98.38%, 84.49% and 91.71% within 30 min, respectively. The k value of SALa/CN (0.10661 min^{-1}) for TC achieves 9.81 times than that of 3DA-CN (0.01087 min^{-1}). Trapping experiments and ESR devices prove that the contribution of active species in the photocatalytic TC removal process is $\bullet\text{O}_2^- > {}^1\text{O}_2 > \text{h}^+ > \text{H}_2\text{O}_2 > \bullet\text{OH}$. This study provides a method for the preparation of rare earth single atom photocatalysts with high loads, and provides a deeper understanding about the mechanism of electron separation for rare earth SALa in space.

CRediT authorship contribution statement

Linlin Sun: Investigation, Methodology, Formal analysis, Data curation, Validation, Conceptualization, Writing – review & editing. **Xiaoshuo Liu:** Methodology, Conceptualization, Data curation, Writing–review & editing. **Yibing Feng:** Investigation, Visualization. **Xunlei Ding:** Validation, Software, Methodology. **Jigang Wang:** Writing – review & editing, Project administration, Funding acquisition. **Nan Jiang:** Methodology, Conceptualization, Visualization. **Shanjiang Wang:** Writing – review & editing, Data curation, Validation.

Declaration of Competing Interest

The authors declare that they have no known competing financial interests or personal relationships that could have appeared to influence the work reported in this paper.

Data Availability

Data will be made available on request.

Acknowledgement

We gratefully acknowledge the financial support of the National Natural Science Foundation of China (21776117), Six Talent Peaks Project in Jiangsu Province (XCL-014) and the Key Project of Tibet Natural Science Foundation (XZ2017ZRG-66(Z)).

Appendix A. Supporting information

Supplementary data associated with this article can be found in the online version at [doi:10.1016/j.apcatb.2023.122979](https://doi.org/10.1016/j.apcatb.2023.122979).

References

- H. Yin, G. Li, X. Chen, W. Wang, P.K. Wong, H. Zhao, T. An, Accelerated evolution of bacterial antibiotic resistance through early emerged stress responses driven by photocatalytic oxidation, *Appl. Catal. B: Environ.* 269 (2020), 118829.
- Y. Cao, R. Wu, Y. Zhou, D. Jiang, W. Zhu, A bioinspired photocatalysis and electrochemiluminescence scaffold for simultaneous degradation and in situ evaluation, *Adv. Funct. Mater.* 32 (2022) 2203005.
- C. Li, Q. Tian, Y. Zhang, Y. Li, X. Yang, H. Zheng, L. Chen, F. Li, Sequential combination of photocatalysis and microalgae technology for promoting the degradation and detoxification of typical antibiotics, *Water Res.* 210 (2022), 117985.
- S. Park, S. Kim, Y. Yea, K. Saravanakumar, E. Lee, Y. Yoon, C.M. Park, Adsorptive and photocatalytic performance of cobalt-doped $\text{ZnTiO}_3/\text{Ti}_3\text{C}_2\text{T}_x$ MXene nanohybrids towards tetracycline: kinetics and mechanistic insight, *J. Hazard. Mater.* 443 (2023), 130165.
- F. Rong, Q. Lu, H. Mai, D. Chen, R.A. Caruso, Hierarchically porous $\text{WO}_3/\text{CdWO}_4$ fiber-in-tube nanostructures featuring readily accessible active sites and enhanced photocatalytic effectiveness for antibiotic degradation in water, *ACS Appl. Mater. Interfaces* 13 (2021) 21138–21148.
- Y. Yu, D. Chen, W. Xu, J. Fang, J. Sun, Z. Liu, Y. Chen, Y. Liang, Z. Fang, Synergistic adsorption-photocatalytic degradation of different antibiotics in seawater by a porous $\text{g-C}_3\text{N}_4/\text{calcined-LDH}$ and its application in synthetic mariculture wastewater, *J. Hazard. Mater.* 416 (2021), 126183.
- Z. Ji, Y. Zhang, X. Qi, Y. Wang, X. Xia, Y. Pei, Low-cost and facile fabrication of recyclable and reusable waste-based geopolymer for visible-light photocatalysis degradation, *J. Clean. Prod.* 310 (2021) 127434.
- Y. Zhao, P. Zhou, J. Lai, W. Zhang, H. Yang, S. Lu, H. Chen, K. Yin, M. Li, L. Tao, C. Shang, M. Tong, S. Guo, $\text{Ni}_{1-x}\text{Co}_x\text{Se}_2/\text{ZnIn}_2\text{S}_4$ hybrid nanocages with strong 2D/2D hetero-interface interaction enable efficient H_2 -releasing photocatalysis, *Adv. Funct. Mater.* 31 (2021) 2100923.
- W. Yang, X.-L. Wang, N. Kong, C. Liu, P. Sun, Z. Wang, Y. Ding, H. Lin, D. Li, T. Wu, Minimized external electric field on asymmetric monolayer maximizes charge separation for photocatalysis, *Appl. Catal. B: Environ.* 295 (2021), 120266.
- M. Song, K. Qi, Y. Wen, X. Zhang, Y. Yuan, X. Xie, Z. Wang, Rational design of novel three-dimensional reticulated $\text{Ag}_2\text{O}/\text{ZnO}$ Z-scheme heterojunction on Ni foam for promising practical photocatalysis, *Sci. Total Environ.* 793 (2021), 148519.
- L. Su, P. Wang, X. Ma, J. Wang, S. Zhan, Regulating local electron density of iron single sites by introducing nitrogen vacancies for efficient photo-fenton process, *Angew. Chem. Int. Ed.* 60 (2021) 21261–21266.
- X.H. Jiang, L.S. Zhang, H.Y. Liu, D.S. Wu, F.Y. Wu, L. Tian, L.L. Liu, J.P. Zou, S. L. Luo, B.B. Chen, Silver single atom in carbon nitride catalyst for highly efficient photocatalytic hydrogen evolution, *Angew. Chem. Int. Ed.* 59 (2020) 23112–23116.
- G. Wang, C.T. He, R. Huang, J. Mao, D. Wang, Y. Li, Photoinduction of Cu single atoms decorated on UiO-66-NH_2 for enhanced photocatalytic reduction of CO_2 to liquid fuels, *J. Am. Chem. Soc.* 142 (2020) 19339–19345.
- L. Sun, Y. Feng, K. Ma, X. Jiang, Z. Gao, J. Wang, N. Jiang, X. Liu, Synergistic effect of single-atom Ag and hierarchical tremella-like $\text{g-C}_3\text{N}_4$: Electronic structure regulation and multi-channel carriers transport for boosting photocatalytic performance, *Appl. Catal. B: Environ.* 306 (2022), 121106.
- Z. Zeng, Y. Su, X. Quan, W. Choi, G. Zhang, N. Liu, B. Kim, S. Chen, H. Yu, S. Zhang, Single-atom platinum confined by the interlayer nanospace of carbon nitride for efficient photocatalytic hydrogen evolution, *Nano Energy* 69 (2020), 104409.
- K. Fujiwara, S.E. Pratsinis, Single Pd atoms on TiO_2 dominate photocatalytic NO_x removal, *Appl. Catal. B: Environ.* 226 (2018) 127–134.
- Z. Zhou, Z. Shen, C. Song, M. Li, H. Li, S. Zhan, Boosting the activation of molecular oxygen and the degradation of tetracycline over high loading Ag single atomic catalyst, *Water Res.* 201 (2021), 117314.
- Y. Yang, F. Li, J. Chen, J. Fan, Q. Xiang, Single Au atoms anchored on amino-group-enriched graphitic carbon nitride for photocatalytic CO_2 reduction, *ChemSusChem* 13 (2020) 1979–1985.
- F. Wang, Y. Wang, Y. Feng, Y. Zeng, Z. Xie, Q. Zhang, Y. Su, P. Chen, Y. Liu, K. Yao, W. Lv, G. Liu, Novel ternary photocatalyst of single atom-dispersed silver and carbon quantum dots co-loaded with ultrathin $\text{g-C}_3\text{N}_4$ for broad spectrum photocatalytic degradation of naproxen, *Appl. Catal. B: Environ.* 221 (2018) 510–520.
- Y. Li, B. Li, D. Zhang, L. Cheng, Q. Xiang, Crystalline carbon nitride supported copper single atoms for photocatalytic CO_2 reduction with nearly 100% CO selectivity, *ACS Nano* 14 (2020) 10552–10561.
- Y. Yang, G. Zeng, D. Huang, C. Zhang, D. He, C. Zhou, W. Wang, W. Xiong, B. Song, H. Yi, S. Ye, X. Ren, In situ grown single-atom cobalt on polymeric carbon nitride with bidentate ligand for efficient photocatalytic degradation of refractory antibiotics, *Small* 16 (2020), e2001634.
- G. Gao, Y. Jiao, E.R. Wacławik, A. Du, Single atom (Pd/Pt) supported on graphitic carbon nitride as an efficient photocatalyst for visible-light reduction of carbon dioxide, *J. Am. Chem. Soc.* 138 (2016) 6292–6297.
- X. Xiao, Y. Gao, L. Zhang, J. Zhang, Q. Zhang, Q. Li, H. Bao, J. Zhou, S. Miao, N. Chen, J. Wang, B. Jiang, C. Tian, H. Fu, A promoted charge separation/transfer system from Cu single atoms and C_3N_4 layers for efficient photocatalysis, *Adv. Mater.* 32 (2020), e2003082.
- M. Ma, Z. Huang, L. Li, W. Zhang, R. Guo, R. Zhang, W. Fa, C. Han, Y. Cao, S. Yu, Y. Zhou, Modulating photogenerated electron density of Pr single-atom sites by coordination environment engineering for boosting photoreduction of CO_2 to CH_3OH , *Appl. Catal. B: Environ.* 330 (2023), 122626.
- J. Liu, X. Kong, L. Zheng, X. Guo, X. Liu, J. Shui, Rare earth single-atom catalysts for nitrogen and carbon dioxide reduction, *ACS Nano* 14 (2020) 1093–1101.
- D. Sun, Y. Chen, X. Yu, Y. Yin, G. Tian, Engineering high-coordinated cerium single-atom sites on carbon nitride nanosheets for efficient photocatalytic amine oxidation and water splitting into hydrogen, *Chem. Eng. J.* 462 (2023), 142084.
- J. Feng, F. Li, X. Li, Y. Wang, D. Fan, B. Du, Y. Li, Q. Wei, Label-free photoelectrochemical immunosensor for NT-proBNP detection based on $\text{La-CdS}/3\text{D ZnIn}_2\text{S}_4/\text{Au}/\text{ZnO}$ sensitization structure, *Biosens. Bioelectron.* 117 (2018) 773–780.
- A. Muhammad, M. Tahir, S.S. Al-Shahrani, A. Mahmood Ali, S.U. Rather, Template free synthesis of graphitic carbon nitride nanotubes mediated by lanthanum (La/g-CNT) for selective photocatalytic CO_2 reduction via dry reforming of methane (DRM) to fuels, *Appl. Surf. Sci.* 504 (2020), 144177.
- T. Jia, M. Liu, C. Zheng, F. Long, Z. Min, F. Fu, D. Yu, J. Li, J.H. Lee, N.H. Kim, One-pot hydrothermal synthesis of La-doped ZnIn_2S_4 microspheres with improved visible-light photocatalytic performance, *Nanomaterials* 10 (2020).
- L. Jing, Y. Xu, J. Liu, M. Zhou, H. Xu, M. Xie, H. Li, J. Xie, Direct Z-scheme red carbon nitride/rod-like lanthanum vanadate composites with enhanced photodegradation of antibiotic contaminants, *Appl. Catal. B: Environ.* 277 (2020), 119245.
- Y. Xie, J. Wu, C. Sun, Y. Ling, S. Li, X. Li, J. Zhao, K. Yang, La_2O_3 -modified graphite carbon nitride achieving the enhanced photocatalytic degradation of different organic pollutants under visible light irradiation, *Mater. Chem. Phys.* 246 (2020), 122846.

- [32] N. Yin, H. Chen, X. Yuan, Y. Zhang, M. Zhang, J. Guo, Y. Zhang, L. Qiao, M. Liu, K. Song, Highly efficient photocatalytic degradation of norfloxacin via $\text{Bi}_2\text{Sn}_2\text{O}_7/\text{PDIH}$ Z-scheme heterojunction: Influence and mechanism, *J. Hazard. Mater.* 436 (2022), 129317.
- [33] Y. Xu, H. Tang, L. Liu, M. Hua, K. Chen, Y. Duan, Hierarchical $\text{Fe}/\text{ZSM-5}$ zeolites for efficient Hg^0 removal from coal-fired flue gas, *Chem. Eng. J.* 450 (2022), 138180.
- [34] X. Ren, M. Xia, B. Chong, X. Yan, N. Wells, G. Yang, Uniform NiP_x nanospheres loaded onto defective $\text{H}_x\text{WO}_{3-y}$ with three-dimensionally ordered macroporous structure for photocatalytic nitrogen reduction, *Appl. Catal. B: Environ.* 297 (2021), 120468.
- [35] L. Sun, X. Liu, X. Jiang, Y. Feng, X. Ding, N. Jiang, J. Wang, An internal electric field and interfacial S-C bonds jointly accelerate S-scheme charge transfer achieving efficient sunlight-driven photocatalysis, *J. Mater. Chem. A* 10 (2022) 25279–25294.
- [36] X. Zu, X. Li, W. Liu, Y. Sun, J. Xu, T. Yao, W. Yan, S. Gao, C. Wang, S. Wei, Y. Xie, Efficient and robust carbon dioxide electroreduction enabled by atomically dispersed Sn^{6+} sites, *Adv. Mater.* 31 (2019), e1808135.
- [37] W. Liu, Y. Chen, H. Qi, L. Zhang, W. Yan, X. Liu, X. Yang, S. Miao, W. Wang, C. Liu, A. Wang, J. Li, T. Zhang, A durable nickel single-atom catalyst for hydrogenation reactions and cellulose valorization under harsh conditions, *Angew. Chem. Int. Ed.* 57 (2018) 7071–7075.
- [38] Z. Jin, Y. Zhang, D. Liu, H. Ding, B.B. Mamba, A.T. Kuvarega, J. Gui, Fabrication of a La-doped BiVO_4/CN step-scheme heterojunction for effective tetracycline degradation with dual-enhanced molecular oxygen activation, *Sep. Purif. Technol.* 277 (2021), 119224.
- [39] Y. Chen, Y. Qu, X. Zhou, D. Li, P. Xu, J. Sun, Phenyl-bridged graphitic carbon nitride with a porous and hollow sphere structure to enhance dissociation of photogenerated charge carriers and visible-light-driven H_2 generation, *ACS Appl. Mater. Interfaces* 12 (2020) 41527–41537.
- [40] J. Liu, M. Jiao, L. Lu, H.M. Barkholtz, Y. Li, Y. Wang, L. Jiang, Z. Wu, D.J. Liu, L. Zhuang, C. Ma, J. Zeng, B. Zhang, D. Su, P. Song, W. Xing, W. Xu, Y. Wang, Z. Jiang, G. Sun, Erratum: High performance platinum single atom electrocatalyst for oxygen reduction reaction, *Nat. Commun.* 8 (2017) 16160.
- [41] W. Zhao, J. Wang, R. Yin, B. Li, X. Huang, L. Zhao, L. Qian, Single-atom Pt supported on holey ultrathin $\text{g-C}_3\text{N}_4$ nanosheets as efficient catalyst for Li-O_2 batteries, *J. Colloid Interf. Sci.* 564 (2020) 28–36.
- [42] M. Zhu, C. Zhao, X. Liu, X. Wang, F. Zhou, J. Wang, Y. Hu, Y. Zhao, T. Yao, L.-M. Yang, Y. Wu, Single atomic cerium sites with a high coordination number for efficient oxygen reduction in proton-exchange membrane fuel cells, *ACS Catal.* 11 (2021) 3923–3929.
- [43] B. Han, T. Li, J. Zhang, C. Zeng, H. Matsumoto, Y. Su, B. Qiao, T. Zhang, A highly active Rh_1/CeO_2 single-atom catalyst for low-temperature CO oxidation, *Chem. Commun.* 56 (2020) 4870–4873.
- [44] J. Gu, M. Jian, L. Huang, Z. Sun, A. Li, Y. Pan, J. Yang, W. Wen, W. Zhou, Y. Lin, H. J. Wang, X. Liu, L. Wang, X. Shi, X. Huang, L. Cao, S. Chen, X. Zheng, H. Pan, J. Zhu, S. Wei, W.X. Li, J. Lu, Synergizing metal-support interactions and spatial confinement boosts dynamics of atomic nickel for hydrogenations, *Nat. Nanotechnol.* 16 (2021) 1141–1149.
- [45] Y. Zhou, W. Lv, B. Zhu, F. Tong, J. Pan, J. Bai, Q. Zhou, H. Qin, Template-free one-step synthesis of $\text{g-C}_3\text{N}_4$ nanosheets with simultaneous porous network and S-doping for remarkable visible-light-driven hydrogen evolution, *ACS Sustain. Chem. Eng.* 7 (2019) 5801–5807.
- [46] L. Sun, X. Liu, X. Jiang, Y. Feng, W. Yang, N. Jiang, J. Wang, Insight into CeO_2 decorated hierarchical tremella-like $\text{Ag}/\text{g-C}_3\text{N}_4$ boosting organic contaminants removal: Maximum redox capacity and local surface plasma resonance effects, *Appl. Surf. Sci.* 599 (2022), 153903.
- [47] Y. Liu, S. Zhang, C. Jiao, H. Chen, G. Wang, W. Wu, Z. Zhuo, J. Mao, Axial phosphate coordination in Co single atoms boosts electrochemical oxygen evolution, *Adv. Sci.* 9 (2022), e2206107.
- [48] A.C. Thenuwara, E.B. Cerkez, S.L. Shumlas, N.H. Attanayake, I.G. McKendry, L. Frazer, E. Borguet, Q. Kang, R.C. Remsing, M.L. Klein, M.J. Zdilla, D.R. Strongin, Nickel confined in the interlayer region of birnessite: an active electrocatalyst for water oxidation, *Angew. Chem. Int. Ed.* 55 (2016) 10381–10385.
- [49] N.H. Attanayake, A.C. Thenuwara, A. Patra, Y.V. Aulin, T.M. Tran, H. Chakraborty, E. Borguet, M.L. Klein, J.P. Perdew, D.R. Strongin, Effect of intercalated metals on the electrocatalytic activity of 1T-MoS_2 for the hydrogen evolution reaction, *ACS Energy Lett.* 3 (2017) 7–13.
- [50] Z. Zeng, X. Quan, H. Yu, S. Chen, W. Choi, B. Kim, S. Zhang, Alkali-metal-oxides coated ultrasmall Pt sub-nanoparticles loading on intercalated carbon nitride: Enhanced charge interlayer transportation and suppressed backwork reaction for overall water splitting, *J. Catal.* 377 (2019) 72–80.
- [51] J. Bian, Y. Liao, R. Liu, X. An, C. Hu, H. Liu, J. Qu, Synergy of cyano groups and cobalt single atoms in graphitic carbon nitride for enhanced bio-denitrification, *Water Res.* 218 (2022), 118465.
- [52] N. Wang, D. Wang, A. Wu, S. Wang, Z. Li, C. Jin, Y. Dong, F. Kong, C. Tian, H. Fu, Few-layered MoS_2 anchored on 2D porous C_3N_4 nanosheets for Pt-free photocatalytic hydrogen evolution, *Nano Res.* 307 (2022) 1–12.
- [53] C. Zhang, D. Qin, Y. Zhou, F. Qin, H. Wang, W. Wang, Y. Yang, G. Zeng, Dual optimization approach to Mo single atom dispersed $\text{g-C}_3\text{N}_4$ photocatalyst: Morphology and defect evolution, *Appl. Catal. B: Environ.* 303 (2022), 120904.
- [54] C. Dong, Z. Zheng, Z. Wang, J. He, Z. Ye, X. Gong, L.M.C. Lo, N-doped graphitic C_3N_4 nanosheets decorated with CoP nanoparticles: A highly efficient activator in single oxygen dominated visible-light-driven peroxymonosulfate activation for degradation of pharmaceuticals and personal care products, *J. Hazard. Mater.* 416 (2021), 125891.
- [55] D. Zhao, C.L. Dong, B. Wang, C. Chen, Y.C. Huang, Z. Diao, S. Li, L. Guo, S. Shen, Synergy of dopants and defects in graphitic carbon nitride with exceptionally modulated band structures for efficient photocatalytic oxygen evolution, *Adv. Mater.* 31 (2019), e1903545.
- [56] G. Li Puma, A. Brucato, Dimensionless analysis of slurry photocatalytic reactors using two-flux and six-flux radiation absorption-scattering models, *Catal. Today* 122 (2007) 78–90.
- [57] J. Xiong, X. Li, J. Huang, X. Gao, Z. Chen, J. Liu, H. Li, B. Kang, W. Yao, Y. Zhu, CN/rGO@BPQDs high-low junctions with stretching spatial charge separation ability for photocatalytic degradation and H_2O_2 production, *Appl. Catal. B: Environ.* 266 (2020), 118602.
- [58] J. Fu, B. Zhu, C. Jiang, B. Cheng, W. You, J. Yu, Hierarchical porous O-doped $\text{g-C}_3\text{N}_4$ with enhanced photocatalytic CO_2 reduction activity, *Small* 13 (2017) 1603938.
- [59] J. Jiang, Z. Xiong, H. Wang, G. Liao, S. Bai, J. Zou, P. Wu, P. Zhang, X. Li, Sulfur-doped $\text{g-C}_3\text{N}_4/\text{g-C}_3\text{N}_4$ isotype step-scheme heterojunction for photocatalytic H_2 evolution, *J. Mater. Sci. Technol.* 118 (2022) 15–24.
- [60] M. Han, C. Kang, Z. Qu, S. Zhu, B. Yang, Surface molecule induced effective light absorption and charge transfer for H_2 production photocatalysis in a carbonized polymer dots-carbon nitride system, *Appl. Catal. B: Environ.* 305 (2022), 121064.
- [61] S. Cao, H. Li, T. Tong, H.-C. Chen, A. Yu, J. Yu, H.M. Chen, Single-atom engineering of directional charge transfer channels and active sites for photocatalytic hydrogen evolution, *Adv. Funct. Mater.* 28 (2018) 1802169.
- [62] H. Che, C. Li, C. Li, C. Liu, H. Dong, X. Song, Benzoyl isothiocyanate as a precursor to design of ultrathin and high-crystalline $\text{g-C}_3\text{N}_4$ -based donor-acceptor conjugated copolymers for superior photocatalytic H_2 production, *Chem. Eng. J.* 410 (2021), 127791.
- [63] X. Zhang, Y. Liu, M. Ren, G. Yang, L. Qin, Y. Guo, J. Meng, Precise carbon doping regulation of porous graphitic carbon nitride nanosheets enables elevated photocatalytic oxidation performance towards emerging organic pollutants, *Chem. Eng. J.* 433 (2022), 134551.
- [64] X. Wang, J. Meng, X. Zhang, Y. Liu, M. Ren, Y. Yang, Y. Guo, Controllable approach to carbon-deficient and oxygen-doped graphitic carbon nitride: Robust photocatalyst against recalcitrant organic pollutants and the mechanism insight, *Adv. Funct. Mater.* 31 (2021) 2010763.
- [65] X. Yu, S.F. Ng, L.K. Putri, L.L. Tan, A.R. Mohamed, W.J. Ong, Point-defect engineering: Leveraging imperfections in graphitic carbon nitride ($\text{g-C}_3\text{N}_4$) photocatalysts toward artificial photosynthesis, *Small* 17 (2021), e2006851.
- [66] M. Moradi, F. Hasanvandian, A.A. Isari, F. Hayati, B. Kakavandi, S.R. Setayesh, CuO and ZnO co-anchored on $\text{g-C}_3\text{N}_4$ nanosheets as an affordable double Z-scheme nanocomposite for photocatalytic decontamination of amoxicillin, *Appl. Catal. B: Environ.* 285 (2021), 119838.
- [67] M. Karpuraranjith, Y. Chen, S. Rajaboopathi, M. Ramadoss, K. Srinivas, D. Yang, B. Wang, Three-dimensional porous MoS_2 nanobox embedded $\text{g-C}_3\text{N}_4/\text{TiO}_2$ architecture for highly efficient photocatalytic degradation of organic pollutant, *J. Colloid Interf. Sci.* 605 (2022) 613–623.
- [68] X. Liang, J. Zhao, T. Wang, Z. Zhang, M. Qu, C. Wang, Constructing a Z-scheme heterojunction photocatalyst of $\text{GaPO}_4/\alpha\text{-MoC}/\text{Ga}_2\text{O}_3$ without mingling type-II heterojunction for CO_2 reduction to CO, *ACS Appl. Mater. Interfaces* 13 (2021) 33034–33044.
- [69] Z. Gao, M. Zhao, G. Yan, H. Huang, W. Yang, X. Ding, C. Wu, I.D. Gates, Identifying the active sites of carbonaceous surface for the adsorption of gaseous arsenic trioxide: A theoretical study, *Chem. Eng. J.* 402 (2020), 125800.
- [70] M. Ma, Z. Huang, R. Wang, R. Zhang, T. Yang, Z. Rao, W. Fa, F. Zhang, Y. Cao, S. Yu, Y. Zhou, Targeted H_2O activation to manipulate the selective photocatalytic reduction of CO_2 to CH_3OH over carbon nitride-supported cobalt sulfide, *Green. Chem.* 24 (2022) 8791–8799.
- [71] X. Xiao, Z. Ruan, Q. Li, L. Zhang, H. Meng, Q. Zhang, H. Bao, B. Jiang, J. Zhou, C. Guo, X. Wang, H. Fu, A unique Fe-N_4 coordination system enabling transformation of oxygen into superoxide for photocatalytic C-H activation with high efficiency and selectivity, *Adv. Mater.* 34 (2022), e2200612.
- [72] Z.Y. Gao, W.J. Yang, X.L. Ding, G. Lv, W.P. Yan, Support effects on adsorption and catalytic activation of O_2 in single atom catalysts with graphene-based substrates, *Phys. Chem. Chem. Phys.* 20 (2018) 7333–7341.
- [73] S. Chen, W.H. Li, W. Jiang, J. Yang, J. Zhu, L. Wang, H. Ou, Z. Zhuang, M. Chen, X. Sun, D. Wang, Y. Li, MOF encapsulating N-heterocyclic carbene-ligated copper single-atom site catalyst towards efficient methane electrosynthesis, *Angew. Chem. Int. Ed.* 61 (2022), e202114450.
- [74] W. Yang, J. Ren, J. Li, H. Zhang, K. Ma, Q. Wang, Z. Gao, C. Wu, I.D. Gates, A novel Fe-Co double-atom catalyst with high low-temperature activity and strong water-resistant for O_3 decomposition: A theoretical exploration, *J. Hazard. Mater.* 421 (2022) 126639.
- [75] Z. Lu, Q. Liang, B. Wang, Y. Tao, Y. Zhao, W. Lv, D. Liu, C. Zhang, Z. Weng, J. Liang, H. Li, Q.-H. Yang, Graphitic carbon nitride induced micro-electric field for dendrite-free lithium metal anodes, *Adv. Energy Mater.* 9 (2019) 1803186.
- [76] J. Li, B. Huang, Q. Guo, S. Guo, Z. Peng, J. Liu, Q. Tian, Y. Yang, Q. Xu, Z. Liu, B. Liu, Van der Waals heterojunction for selective visible-light-driven photocatalytic CO_2 reduction, *Appl. Catal. B: Environ.* 284 (2021), 119733.
- [77] L. Sun, Y. Qi, C.J. Jia, Z. Jin, W. Fan, Enhanced visible-light photocatalytic activity of $\text{g-C}_3\text{N}_4/\text{Zn}_2\text{GeO}_4$ heterojunctions with effective interfaces based on band match, *Nanoscale* 6 (2014) 2649–2659.
- [78] B. Zhu, J. Zhang, C. Jiang, B. Cheng, J. Yu, First principle investigation of halogen-doped monolayer $\text{g-C}_3\text{N}_4$ photocatalyst, *Appl. Catal. B: Environ.* 207 (2017) 27–34.
- [79] Y. Zhou, C. Zhang, D. Huang, W. Wang, Y. Zhai, Q. Liang, Y. Yang, S. Tian, H. Luo, D. Qin, Structure defined 2D $\text{Mo}_2\text{C}/2\text{D g-C}_3\text{N}_4$ Van der Waals heterojunction: oriented charge flow in-plane and separation within the interface to collectively

- promote photocatalytic degradation of pharmaceutical and personal care products, *Appl. Catal. B: Environ.* 301 (2022), 120749.
- [80] L. Sun, W. Wang, C. Zhang, M. Cheng, Y. Zhou, Y. Yang, H. Luo, D. Qin, C. Huang, Z. Ouyang, Multiple optimization strategies for improving photocatalytic performance of the h-BN/flower-ring g-C₃N₄ heterostructures: morphology engineering and internal electric field effect, *Chem. Eng. J.* 446 (2022), 137027.
- [81] J. Han, Z. Zhu, N. Li, D. Chen, Q. Xu, H. Li, J. He, J. Lu, Metalloporphyrin-based D-A type conjugated organic polymer nanotube for efficient photocatalytic degradation, *Appl. Catal. B: Environ.* 291 (2021), 120108.
- [82] L. Jiang, X. Yuan, G. Zeng, X. Chen, Z. Wu, J. Liang, J. Zhang, H. Wang, H. Wang, Phosphorus- and Sulfur-Codoped g-C₃N₄: Facile preparation, mechanism insight, and application as efficient photocatalyst for tetracycline and methyl orange degradation under visible light irradiation, *ACS Sustain. Chem. Eng.* 5 (2017) 5831–5841.
- [83] C. Feng, Z. Chen, J. Jing, J. Hou, The photocatalytic phenol degradation mechanism of Ag-modified ZnO nanorods, *J. Mater. Chem. C* 8 (2020) 3000–3009.
- [84] H. Ma, X. Wang, T. Tan, X. Zhou, F. Dong, Y. Sun, Stabilize the oxygen vacancies in Bi₂SiO₅ for durable photocatalysis via altering local electronic structure with phosphate dopant, *Appl. Catal. B: Environ.* 319 (2022), 121911.
- [85] T. Xie, Y. Zhang, W. Yao, Y. Liu, H. Wang, Z. Wu, Synthesis of Bi-deficient monolayered Bi₂WO₆ nanosheets with enhanced photocatalytic activity under visible light irradiation, *Catal. Sci. Technol.* 9 (2019) 1178–1188.
- [86] Q. Su, J. Li, B. Wang, Y. Li, La Hou, Direct Z-scheme Bi₂MoO₆/UiO-66-NH₂ heterojunctions for enhanced photocatalytic degradation of ofloxacin and ciprofloxacin under visible light, *Appl. Catal. B: Environ.* 318 (2022), 121820.
- [87] J. Song, X. Yuan, M. Sun, Z. Wang, G. Cao, K. Gao, C. Yang, F. Zhang, F. Dang, W. Wang, Oxidation of tetracycline hydrochloride with a photoenhanced MIL-101 (Fe)/g-C₃N₄/PMS system: Synergetic effects and radical/nonradical pathways, *Ecotox. Environ. Safe* 251 (2023), 114524.
- [88] A. Wang, Z. Zheng, H. Wang, Y. Chen, C. Luo, D. Liang, B. Hu, R. Qiu, K. Yan, 3D hierarchical H₂-reduced Mn-doped CeO₂ microflowers assembled from nanotubes as a high-performance Fenton-like photocatalyst for tetracycline antibiotics degradation, *Appl. Catal. B: Environ.* 277 (2020), 119171.